# Geologic history of Martian regolith breccia Northwest Africa 7034: Evidence for hydrothermal activity and lithologic diversity in the Martian crust

Francis M. Mccubbin, Jeremy W. Boyce, Tímea Novák-Szabó, Alison R. Santos, Romain Tartèse, Nele Muttik, Gabor Domokos, Jorge Vazquez, Lindsay P. Keller, Desmond E. Moser, et al.

AGU PUBLICATIONS

JGR

Journal of Geophysical Research: Planets

RESEARCH ARTICLE
10.1002/2016JE005143

**Key Points:**
- The Martian breccia NWA 7034 is an air fall deposit that was likely formed by impact processes on Mars
- The earliest crust on Mars formed through alkali-rich volcanism under oxidizing conditions
- Regolith formation processes on Mars were driven by impact/volcanic processes, whereby unconsolidated materials were fused together at high T

**Supporting Information:**
- Supporting Information S1
- Tables S1–S8

**Correspondence to:**
F. M. McCubbin,
francis.m.mccubbin@nasa.gov

**Citation:**
McCubbin, F. M., et al. (2016), Geologic history of Martian regolith breccia Northwest Africa 7034: Evidence for hydrothermal activity and lithologic diversity in the Martian crust, *J. Geophys. Res. Planets*, *121*, 2120–2149, doi:10.1002/2016JE005143.

Received 27 JUL 2016
Accepted 19 SEP 2016
Accepted article online 24 SEP 2016
Published online 18 OCT 2016



# Geologic history of Martian regolith breccia Northwest Africa 7034: Evidence for hydrothermal activity and lithologic diversity in the Martian crust

**Francis M. McCubbin[1,2], Jeremy W. Boyce[2,3], Tímea Novák-Szabó[4,5], Alison R. Santos[2], Romain Tartèse[6,7], Nele Muttik[2], Gabor Domokos[4], Jorge Vazquez[8,9], Lindsay P. Keller[1], Desmond E. Moser[10], Douglas J. Jerolmack[5], Charles K. Shearer[2], Andrew Steele[11], Stephen M. Elardo[11], Zia Rahman[12], Mahesh Anand[7,13], Thomas Delhaye[14], and Carl B. Agee[2]**

[1]NASA Johnson Space Center, Houston, Texas, USA, [2]Institute of Meteoritics, University of New Mexico, Albuquerque, New Mexico, USA, [3]Department of Earth, Planetary, and Space Sciences, University of California, Los Angeles, California, USA, [4]Department of Mechanics, Materials, and Structures, Budapest University of Technology and Economics, Budapest, Hungary, [5]Department of Earth and Environmental Science, University of Pennsylvania, Philadelphia, Pennsylvania, USA, [6]Institut de Minéralogie, de Physique des Matériaux et de Cosmochimie, Muséum National d'Histoire Naturelle, Sorbonne Universités, CNRS, UPMC, and IRD, Paris, France, [7]Department of Physical Sciences, The Open University, Walton Hall, UK, [8]U.S. Geological Survey, Menlo Park, California, USA, [9]Stanford-USGS Ion Microprobe Laboratory, Stanford University, Stanford, California, USA, [10]Department of Earth Sciences, University of Western Ontario, London, Ontario, Canada, [11]Geophysical Laboratory, Carnegie Institution of Washington, Washington, DC, USA, [12]Science Department, Jacobs—NASA Johnson Space Center, Houston, texas, USA, [13]Department of Earth Sciences, Natural History Museum, London, UK, [14]Plateforme NanoSIMS, OSUR, Université de Rennes 1, CNRS UMR 6118, Rennes, France

**Abstract** The timing and mode of deposition for Martian regolith breccia Northwest Africa (NWA) 7034 were determined by combining petrography, shape analysis, and thermochronology. NWA 7034 is composed of igneous, impact, and brecciated clasts within a thermally annealed submicron matrix of pulverized crustal rocks and devitrified impact/volcanic glass. The brecciated clasts are likely lithified portions of Martian regolith with some evidence of past hydrothermal activity. Represented lithologies are primarily ancient crustal materials with crystallization ages as old as 4.4 Ga. One ancient zircon was hosted by an alkali-rich basalt clast, confirming that alkalic volcanism occurred on Mars very early. NWA 7034 is composed of fragmented particles that do not exhibit evidence of having undergone bed load transport by wind or water. The clast size distribution is similar to terrestrial pyroclastic deposits. We infer that the clasts were deposited by atmospheric rainout subsequent to a pyroclastic eruption(s) and/or impact event(s), although the ancient ages of igneous components favor mobilization by impact(s). Despite ancient components, the breccia has undergone a single pervasive thermal event at 500–800°C, evident by groundmass texture and concordance of ~1.5 Ga dates for bulk rock K-Ar, U-Pb in apatite, and U-Pb in metamict zircons. The 1.5 Ga age is likely a thermal event that coincides with rainout/breccia lithification. We infer that the episodic process of regolith lithification dominated sedimentary processes during the Amazonian Epoch. The absence of pre-Amazonian high-temperature metamorphic events recorded in ancient zircons indicates source domains of static southern highland crust punctuated by episodic impact modification.

## 1. Introduction

The history of a planetary body such as Mars is recorded within its rock record. Each rock type provides insights into different aspects of planetary evolution, with sedimentary rocks capable of recording a rich history of surface processes, as well as past biologic, geologic, and climatic activities. The surface and crust of Mars have been the focus of intensive study by orbital spectroscopic observations and in situ surface analysis by landers and rovers [e.g., *Bibring et al.*, 2005, 2006; *Carr*, 2007; *Christensen et al.*, 2005; *Ehlmann et al.*, 2008; *Grotzinger and Milliken*, 2012; *McEwen et al.*, 2011; *McLennan et al.*, 2005; *McSween et al.*, 1999, 2004; *Murchie et al.*, 2007; *Poulet et al.*, 2005; *Squyres et al.*, 2004; *Stolper et al.*, 2013]. Additionally, there have been many detailed analytical investigations of Martian meteorites [e.g., *Borg and Draper*, 2003; *Brandon et al.*, 2012; *Day et al.*, 2006; *Dyar et al.*, 2005; *Greenwood et al.*, 2008; *Herd et al.*, 2002; *McCubbin et al.*, 2013; *McKay et al.*, 1996; *McSween and Treiman*, 1998; *Monkawa et 9al.*, 2006; *Nyquist et al.*, 2001; *Papike et al.*, 2009; *Sarbadhikari et al.*, 2009; *Shearer et al.*, 2013; *Steele et al.*, 2012; *Treiman*, 2005; *Usui et al.*, 2008; *Wadhwa*,

2001] as well as experimental studies that have simulated Martian conditions in the laboratory [e.g., *Adcock et al.*, 2013; *Collinet et al.*, 2015; *Dreibus et al.*, 2008; *Filiberto*, 2008; *Filiberto and Dasgupta*, 2011; *Filiberto et al.*, 2010a, 2010b; *Golden et al.*, 2005; *Hurowitz et al.*, 2005; *McCanta et al.*, 2004; *McCubbin et al.*, 2008; *McSween et al.*, 2001; *Medard and Grove*, 2006; *Monders et al.*, 2007; *Musselwhite et al.*, 2006; *Nekvasil et al.*, 2009; *Papike et al.*, 2013]. These studies have shown that the planet Mars has had a complex geologic history. The sedimentary rock record of Mars indicates that sedimentary units are typically sourced from basaltic igneous rocks [*McLennan et al.*, 2014; *McSween et al.*, 2009; *Squyres and Knoll*, 2005; *Squyres et al.*, 2006; *Taylor and McLennan*, 2008]. This characteristic of Martian sediments marks an important contrast between sedimentary environments on Earth and those on Mars [*McLennan*, 2012; *Tosca and McLennan*, 2006]. Furthermore, the apparent absence of plate tectonics on Mars indicates that the entire range of geologic activities and paleoenvironments that have existed on Mars is potentially preserved in the rock record at or near the Martian surface on billion-year time scales [*Grotzinger and Milliken*, 2012; *Malin and Edgett*, 2000].

Despite the abundance of sediments on the Martian surface [*Malin and Edgett*, 2000; *McLennan et al.*, 2005, 2014; *Szabó et al.*, 2015], Martian sedimentary rocks are not represented in the inventory of meteorites with the exception of a single sample, Northwest Africa (NWA) 7034 [*Agee et al.*, 2013], and its pairings, e.g., NWA 7533, NWA 7475, NWA 7906, NWA 7907, NWA 8114, and NWA 8171. NWA 7034 is a polymict regolith breccia with a basaltic bulk composition [*Agee et al.*, 2013; *Humayun et al.*, 2013; *Wittmann et al.*, 2015] that closely matches estimates for the bulk-crust composition of Mars [*Agee et al.*, 2013; *McCubbin et al.*, 2015; *McSween et al.*, 2009; *Taylor and McLennan*, 2008]. Furthermore, NWA 7034 yields a better match than any other Martian meteorite to visible-infrared reflectance spectra of the Martian surface measured from orbit [*Beck et al.*, 2015; *Cannon et al.*, 2015]. Although bulk-rock measurements of NWA 7034 have uncovered important new interpretations regarding the composition of the Martian atmosphere and the origin of crustal magnetic signatures [*Cartwright et al.*, 2014; *Gattacceca et al.*, 2014], detailed textural studies of the meteorite have focused upon the igneous or impact history of the breccia [*Bellucci et al.*, 2015; *Humayun et al.*, 2013; *Lorand et al.*, 2015; *Nemchin et al.*, 2014; *Santos et al.*, 2015; *Udry et al.*, 2014; *Wittmann et al.*, 2015]. Consequently, its potential utility for recording Martian sedimentary processes has gone largely unrecognized, despite it being our first regolith breccia from an extraterrestrial body with an atmosphere. In the present study, we examine the textural, temporal, and spatial relationships among all of the matrix and clast components within NWA 7034 to determine the surface processes that were required for its formation, including its deposition and subsequent lithification, and their timing. This information is subsequently used to place better constraints on Martian crustal evolution.

## 2. Analytical Methods

A textural and mineralogical examination of NWA 7034 was conducted by optical microscopy, scanning electron microscopy, transmission electron microscopy, and Raman microspectral imaging to investigate petrological and mineralogical textures of clasts, mineral fragments, and matrix materials from the centimeter to submicron scales. Furthermore, minerals that can yield age information (i.e., zircon, apatite, and baddeleyite) were identified and analyzed for major, minor, and trace elements by electron probe microanalysis and secondary ion mass spectrometry. These detailed petrography and geochronology are combined with mineral closure temperatures and quantitative shape analysis of clasts and mineral fragments to reconstruct the geologic history of regolith breccia NWA 7034.

### 2.1. Scanning Electron Microscopic Imaging and Identification of Zr-Rich Phases

Back-scattered electron (BSE) images and X-ray maps of whole polished thin sections of NWA 7034 were acquired by using a FEI Quanta 3D-FEG dual-beam focused ion beam (FIB) scanning electron microscope (SEM) at the Open University, UK, fitted with an Oxford Instruments INCA energy dispersive X-ray detector. For this purpose, sections were carbon-coated and examined with an electron beam current of 0.6 nA at an accelerating voltage of 20 keV. We used the whole-section X-ray maps of Zr and P to locate Zr-bearing minerals and apatites, respectively. Given the low resolution at which the samples were mapped, we could only identify Zr-rich phases and phosphates that were larger than about 20 μm. Subsequently, we acquired high-magnification BSE images of areas containing the Zr-bearing minerals and apatites. Semiquantitative

energy dispersive spectra (EDS) were recorded on each phase to check the chemical compositions to aid in phase identity.

To determine the distribution of Zr-rich mineral grains in NWA 7034, a Hitachi SU6600 field emission (FE)-SEM housed at the University of Western Ontario was used to identify and locate zircon, baddeleyite in carbon-coated thick and thin sections. The instrument is equipped with Oxford INCA-Feature software and an XMax large area silicon drift detector. The sample surface was subdivided in tiles at 150X magnification and mapped at beam voltage of 15 keV and a working distance of 10 mm. Beam rastering of the tiles allowed identification of grains as small as 1 μm using the criteria of (1) preset BSE intensity range and (2) EDS spectra acquired by using a dwell time of several seconds. This high-resolution zircon and baddeleyite mapping provided better constraints on the distribution of Zr-rich phases in NWA 7034 than the low-resolution mapping we conducted by using the FEI Quanta 3D-FEG dual beam focused ion beam (FIB) scanning electron microscope (SEM). Grain dimensional data and stage coordinates were recorded, and then symbolized by using an ArcMAP platform following manual data quality assessment. Note that in the population of the smallest zircon grains, a minor component (estimated 10%) could be misidentified as baddeleyite as these grains approach the ~1 μm diameter of the EDS activation volume, and hence, Si from the matrix may appear in the target spectrum. Full details of these methods are available in *Moser et al*. [2013].

### 2.2. Focused Ion Beam and Transmission Electron Microscopy

Detailed mineralogical, structural, and textural characterization of five regions of interest within the NWA 7034 groundmass were selected to understand the variety of submicron textures exhibited among the various macroscale (i.e., identified through petrographic analysis) textural regimes in NWA 7034, including the bulk matrix domain (i.e., the interconnected groundmass that is interstitial to the clasts in NWA 7034) and interfaces between the bulk matrix domain and various clast types in NWA 7034. These regions of interest were investigated by transmission electron microscopy (TEM) at NASA Johnson Space Center (JSC). Prior to TEM work, cross sections were extracted from the NWA 7034 thin section by an in situ lift-out technique by using the FEI Quanta 3D-FEG scanning electron microscopeed (FIB) instrument at NASA JSC. Prior to the FIB section preparation, the samples were coated with carbon. A high-quality carbon layer of 30 to 100 nm provides some initial surface protection to ion milling and makes the sample conductive. The sample was inserted into the SEM/FIB instrument along with a TEM Cu-grid by standard SEM sample mounting techniques to provide a conductive bulk sample in the FIB. After locating the exact region of interest, an additional protective layer of 2 μm wide and 2 μm thick carbon was deposited as a strip across the area of interest prior to FIB sample preparation to minimize ion beam damage. Trenches, about 5 μm wider than the carbon strip, were milled on either side of the carbon-coated region at 52° stage tilt or 90° angle with respect to the ion beam, leaving a region of interest as a slice about 3 μm in thickness. The trenches were milled sufficiently deep below the region of interest in order to avoid the ion beam damage of the next milling steps to the area. The exposed section was cut partially free by milling the sides and the bottom of the section at 7° stage tilt using the primary ion beams to release the sample by a tungsten needle. The specimen was welded to the needle and milled free from the substrate at 0° stage tilt. The extracted slice was lifted out by using a micromanipulator and mounted onto a TEM grid for final FIB thinning to electron transparency (approximately 60 nm thick). In the following step, the specimen was thinned from both sides gradually by using a 30 keV ion beam and a current of 30 pA. In order to avoid damage in the final lamella, the ion-beam energy was progressively lowered during the process down to low-keV milling (about 2 keV) at the final stage of cleaning on both sides of the specimen.

The FIB sections were characterized in detail by using bright-field (BF) and darkfield (DF) images, high-resolution (HR) images, and selected area electron diffraction (SAED) obtained by using a JEOL 2500SE field emission scanning transmission electron microscope (FE-STEM) equipped with a Noran thin window energy-dispersive X-ray (EDX) spectrometer operating at 200 keV. Digital TEM images were acquired and processed by using GATAN Digital Microscopy Suite® imaging software. BF and DF imaging was carried out across the entire area of each section at different magnifications by using the high-angle annular darkfield (HAADF) detector that allows chemically sensitive imaging. The BF detector collects the same signal as the TEM bright-field image and exhibits largely crystallographic information; however, if electrons scattered to high angles (larger than the low-index Bragg reflections) are primarily collected, an annular darkfield (ADF) image is acquired. The HAADF signal is directly proportional to the density and thickness of the specimen and

proportional to $Z^{3/2}$, where Z is the atomic number, meaning the heavier the atom, the higher the intensity of the scattering, which leads to atomic number (Z) contrast in the image. In addition, SAED and EDX were carried out on each phase to measure its chemical composition. SAED patterns were measured for the phase identification and verified by comparing the measured SAED patterns to known structure types. Elemental distributions were obtained by EDS X-ray intensity maps by using STEM raster mode with scanned probe sizes of 2 nm and a dwell time of 50 μs/pixel to limit beam damage and element diffusion during the experiments. The size of the rastered area was typically 256 × 204 pixels at a magnification that was optimized to limit over or undersampling with the 2 nm probe. The large solid angle of the microscope combined with a large active area detector results in spectrum images where each pixel in spectrum images contain a full high-count EDX spectrum that enables one to determine the quantitative element abundances in addition to displaying the spatial distribution of major and minor elements. Successive image layers of each region were acquired and combined in order to achieve better than 10% counting statistics for major elements in each pixel. Quantitative abundances for the mineral phases and element line (zoning) profiles were extracted from the spectrum images. Data reduction was performed by using the Cliff-Lorimer thin film approximation with experimental K-factors determined from a variety of standards.

### 2.3. Electron Probe Microanalysis of Zircon, Baddeleyite, and Apatite

Major and minor element abundances of zircon, baddeleyite, and apatite were determined by using the JEOL 8200 Superprobe run by the Probe for EPMA software at the Institute of Meteoritics, University of New Mexico. All of the zircon and baddeleyite analyses were collected on a single sample of NWA 7034, University of New Mexico (UNM) section 2,2. Zircon and baddeleyite were analyzed with a 15 keV accelerating voltage, 30 nA beam current, and a 3–5 μm beam diameter. Count times were 30 s on peak for major elements and 60 s on peak for minor elements, and backgrounds were counted for half the peak counting time. Standards were a mix of both natural and synthetic minerals and oxides. All apatites were analyzed by using a 15 keV accelerating voltage, 20 nA beam current, and a 3–10 μm beam diameter following previous procedures and standardizations established by our group for the analysis of apatite in planetary materials by electron microprobe [i.e., *McCubbin et al*., 2010, 2011, 2013]. We also used the JEOL 8200 Superprobe to collect BSE images of apatites and zircons that were analyzed by secondary ion mass spectrometry (SIMS) using the same beam conditions as those described above for the analysis of zircon, baddeleyite, and apatite, respectively.

### 2.4. Wavelength Dispersive Spectroscopic X-ray Imaging

Qualitative X-ray map of Clast 78 and its immediate surroundings from *Santos et al*. [2015] were collected by using the JEOL 8200 Superprobe run by the Probe for EPMA software located at the Institute of Meteoritics, University of New Mexico. Qualitative $K_\alpha$ X-ray maps were made in a single accumulation by utilizing five wavelength dispersive spectroscopic spectrometers simultaneously. $K_\alpha$ X-ray maps of Mg, Ti, Si, Ca, and Fe were made at an accelerating voltage of 15 keV and a beam current of 30 nA. Dwell times were 100 ms, and pixel sizes were 1 μm. Resultant maps were interpolated, and the color contrast was adjusted in some cases to best show the details of the zoning patterns and elemental distributions. Therefore, identical color levels in the maps presented here are not necessarily correlated to identical concentrations in maps of the same element in different regions.

### 2.5. Raman Spectroscopy and Multispectral Imaging

In order to determine the identity of the ferric oxides associated with pyrite in NWA 7034, Raman spectra and images were collected at the Geophysical Laboratory, Carnegie Institution of Washington, using a Witec α-Scanning Near-Field Optical Microscope that has been customized to incorporate confocal Raman spectroscopic imaging. The excitation source is a frequency-doubled solid-state yttrium/aluminum/garnet laser (532 nm) operating between 0.3 and 1 mW output power (dependent on objective), as measured at the sample by using a laser power meter. Objective lenses used included a 100X long working distance (LWD) and a 20X LWD with a 50 μm optical fiber acting as the confocal pinhole. Spectra were collected on an Peltier-cooled Andor Electron Multiplying Charge Coupled Device chip, after passing through an *f*/4 300 mm focal length imaging spectrometer typically by using a 600 lines per millimeter grating. The lateral resolution of the instrument is as small as 360 nm in air when using the 100X LWD objective, with a focal plane depth of ~800 nm.

This instrument is capable of operating in several modes. Typically, 2-D imaging and single spectra modes were used during this study. Single spectra mode allows the acquisition of a spectrum from a single spot on the target. Average spectra are produced typically by using integration times of 30 s per accumulation and 10 accumulations to allow verification of weak spectral features.

The pyrite-rich target areas were identified on the thin section by using both transmitted and reflected light. Before analysis, the microscope was switched to reflected light and refocused to the surface, at which point X, Y, and Z piezos of the stage were reset. Switching back to transmitted light then allows an accurate measurement of the depth of the feature of interest. The height and width of the field of interest within the light microscopy image were then measured and divided by the lateral resolution of the lens being used to give the number of pixels per line. The instrument then takes a Raman spectrum (0–3600 $cm^{-1}$ using the 600 lines per millimeter grating) at each pixel using an integration time of between 1 and 6 s per pixel. A cosmic ray reduction routine was used to reduce the effects of stray radiation on Raman images, as was image thresholding to reject isolated bright pixels. Fluorescence effects were inhibited by the use of specific peak fitting in place of spectral area sums and by the confocal optics used in this instrument. This produces an average spectrum over the number of pixels chosen in the area of interest. In a typical scan at 100X of a 30 $\mu m^2$ area, $100 \times 100$ pixels were scanned amounting to 10,000 separate and spatially aligned Raman spectra, from which average spectra from areas of interest were generated to ascertain the presence or absence of a certain peak. Standard spectra of hematite, göethite, magnetite, and maghemite were obtained from the papers of *Wang et al*. [2004a, 2004b] and *Cooney et al*. [1999] as well as an internal Raman database and the database provided by the RRUFF project (www.rruff.info).

### 2.6. Sensitive High-Resolution Ion Microprobe - Reverse Geometry U-Pb Dating and Trace Element Analysis of Zircon

Zircon U-Pb and trace element analyses were performed by using the Stanford-U.S. Geological Survey (USGS) Sensitive High-Resolution Ion Microprobe - Reverse Geometry (SHRIMP-RG) ion microprobe housed at Stanford University. For U-Pb analyses of zircon, a primary beam of mass-filtered negative $O_2$ ions was focused to an ~15 μm diameter spot with Köhler illumination and an intensity of ~2.5 nA. The zircon sample surface was rastered for 2 min prior to measurement of secondary ions to reduce/remove surface contamination. Positive secondary ions of $^{90}Zr_2{}^{16}O$, $^{204}Pb$, $^{206}Pb$, $^{207}Pb$, $^{208}Pb$, $^{238}U$, $^{232}Th^{16}O$, and $^{238}U^{16}O$ were measured by peak hopping using a discrete dynode electron multiplier. The exit and collector slits of the mass spectrometer were adjusted to achieve a mass resolution of 7000 at 10% peak height. Raw data were corrected for background and 25 ns collector deadtime, and reduced using Squid 2.51 [*Ludwig*, 2009] software. Measured Pb/U ratios are corrected by using a $^{206}Pb^+/^{238}U^+$-$^{238}U^{16}O^+/^{238}U^+$ calibration relation [*Claoué-Long et al*., 1995] with calibration to the 1096 Ma AS3 standard zircon [*Schoene et al*., 2006]. Analyses of Temora-2 zircon on a separate mount during the U-Pb session for NWA 7034 zircon yield a $^{207}Pb$-corrected age of 426 ± 8 Ma (95% confidence, $n = 10/10$, mean square weighted deviate (MSWD) = 1.4), which agrees well with an age of 418.4 ± 0.1 Ma from thermal ionization mass spectrometry [*Mattinson*, 2010]. $^{235}U/^{207}Pb$ ratios are calculated assuming $^{238}U/^{235}U = 137.82$ [*Hiess et al*., 2012]. Dates were calculated by using Isoplot v. 3.7 [*Ludwig*, 2008]. Common Pb-corrected ratios and dates assume a modern composition from *Stacey and Kramers* [1975] and that common Pb is derived from surface/fracture contamination of the zircon during mount preparation. Trace element analyses of zircon were conducted separately from the U-Pb dating using the acquisition protocol described in *Grimes et al*. [2007], with a 2.5 nA primary beam of negative $O_2$ ions, and with the mass spectrometer tuned for a mass resolution of 10,500 to resolve potential interferences. Reported concentrations for trace elements are calculated by using secondary ion intensities normalized to $^{30}Si^+$ with calibration to zircon standards 91500 (rare earth element (REE), P, Nb, Hf, Pb, U, and Th) and SL-13 (Ti) using values from *Wiedenbeck et al*. [1995, 2004], and *Hiess et al*. [2008].

### 2.7. SHRIMP-RG U-Pb and Pb-Pb Dating and Trace Element Analysis of Apatite

U-Pb analyses of apatite were conducted with the Stanford-USGS SHRIMP-RG ion microprobe by using an ~5.0 nA primary beam of negative $O_2$ ions. The sample surface was rastered for 60 s prior to measurement of secondary ions. The mass analyzer was tuned for mass resolution of ~8000 in order to resolve potential isobaric interferences. Similar to the protocol for zircon analyses, measured U/Pb ratios for apatite were corrected with a $UO^+/U^+$-$Pb^+/U^+$ calibration scheme as described by *Terada and Sano* [2012] and using the

MAD1 apatite standard dated at 487 Ma by isotope dilution thermal ionization mass spectrometry [*Thomson et al*., 2012]. Raw data were corrected for background and 25 ns collector deadtime, and reduced using Squid 2.51 [*Ludwig*, 2009] software. Trace element concentrations were determined by using secondary ion yields normalized to $^{40}Ca_2{}^{31}P^{16}O_3{}^+$ [*Terada and Sano*, 2003] and calibrated to Durango apatite by using the concentrations reported by *Sha and Chappell* [1999].

### 2.8. NanoSIMS 50 U-Pb and Pb-Pb Dating of Zircon and Baddeleyite

U-Pb analyses of zircon and baddeleyite grains were carried out by using the Cameca NanoSIMS 50 installed at the University of Rennes 1, France. A general description of the instrument and its configuration for dating purposes is given in *Tartèse et al*. [2013]. For this analytical session, the $O^-$ beam was optimized by using apertures D0-1 and D1-1, and two different tuning parameters were set in order to produce currents of ~40 pA and ~1 nA, used for imaging and spot analysis, respectively. The vacuum in the analysis chamber remained constant for the whole session at $\sim 4 \times 10^{-9}$ torr. Before punctual analysis, secondary ion images of the distribution of $^{89}Y$, $^{90}Zr_2{}^{16}O$, $^{180}Hf$, and $^{238}U^{16}O$ were acquired in order to examine potential zoning features in the zircon grains. Areas of interest were divided into 256 pixels × 256 pixels ion images. $^{89}Y$ and $^{90}Zr_2{}^{16}O$ were first acquired with a dwell time of 2 ms/pixel, and $^{180}Hf$ and $^{238}U^{16}O$ were then acquired with a dwell time of 15 ms/pixel, resulting in a total acquisition time of ~18 min 30 s. The data were processed off-line by using the OpenMIMS software (National Institutes of Health/National Institute of Biomedical Imaging and Bioengineering (NIH/NIBIB) National Resource for Imaging Mass Spectrometry, NIH/NIBIB 5P41 EB001974-10).

For U-Pb isotope analysis, the primary beam was rastered over 2 μm × 2 μm or 3 μm × 3 μm areas, depending on the target size and zoning features. Secondary ions emitted from the sample were extracted through the entrance (ES) and aperture (AS) slits. In this study, we used ES-3 and AS-1, which resulted in a net relative transmission of secondary ions of 40% and allowed us to achieve a mass resolving power of ~5000 (Cameca definition, equivalent to a mass resolution of ~3500), sufficient to isolate the major HfSi interferences from the Pb isotopes. Analyses were carried out by using the NanoSIMS combined mode: the magnetic field was switched to measure background (203.5), $^{204}Pb$, $^{206}Pb$, and $^{207}Pb$ in an up-mass sequence in the detector EM#2, and species $^{90}Zr_2{}^{16}O$, $^{238}U$, and $^{238}U^{16}O$ were simultaneously acquired on the other detectors together with $^{206}Pb$. Waiting time between each field switching was set to 0.5 s. Before analysis, the probe was rastered over a 6 μm × 6 μm area for ~5 min to remove any potential surface contamination. Secondary ions were then collected for 14 cycles of the sequence described above, resulting in a total analysis time of ~23 min. Automatic centering was performed on the $^{90}Zr_2{}^{16}O$ peak at the beginning of each analysis and repeated halfway through each run. The secondary ion signals were processed by using the NanoSIMS DataEditor software developed by Frank Gyngard (Washington University, St Louis, USA), and isotope ratios were calculated from total counts.

The measured Pb/U ratios were corrected by using a $^{206}Pb^+/^{238}U^+$-$^{238}U^{16}O^+/^{238}U^+$ calibration relation [*Claoué-Long et al*., 1995] with calibration to the 1065 Ma 91500 standard zircon [*Wiedenbeck et al*., 1995]. The best fit line corresponded to a power law relationship with an exponent of ~2.2, which is consistent with the proposition of *Claoué-Long et al*. [1995] that the exponent should be around 2. Similarly, U and Pb concentrations in unknown samples were derived from the relationship relating the measured $^{206}Pb^+/Zr_2O^+$ and $UO^+/U^+$ ratios in the 91500 reference zircon (U = 80 ppm, Pb = 15 ppm). All the Pb isotopes have been corrected for common Pb contribution using the measured $^{204}Pb/^{206}Pb$ ratios and a present-day common Pb composition using the two-stage model of *Stacey and Kramers* [1975]. This procedure assumes that all the measured $^{204}Pb$ has been introduced in the sample while it was residing on Earth's surface or during sample handling and preparation. We applied the same protocol for baddeleyite U-Pb dating, using the 2060 Ma Phalaborwa baddeleyite (U ~ 530 ppm, Pb ~ 200 ppm [*Heaman*, 2009]) as our reference material. However, baddeleyite U-Pb dating by SIMS is hampered by large and unpredictable U and Pb fractionations due to crystal orientation effects [*Wingate and Compston*, 2000]. As a result, we only report the $^{207}Pb/^{206}Pb$ dates corrected for common Pb contributions. Nine analyses carried out on the Phalaborwa baddeleyite yielded a weighted mean $^{207}Pb/^{206}Pb$ date of 2071 ± 33 Ma (2 s, MSWD = 0.84), consistent with its recommended crystallization age of 2060 Ma [*Heaman*, 2009]. All the final date calculations were carried out by using the Isoplot 3.7 add-in for Excel [*Ludwig*, 2008].

## 3. Shape and Size Analysis of Clasts

### 3.1. Image Analysis

To constrain the depositional processes of the components that make up the NWA 7034 breccia, we analyzed the shape and the size distributions of various clast types that were identified based on compositional and textural differences, including igneous textured clasts, mineral clasts, melt clasts, and protobreccia clasts (Figures 1 and S1–S4 in the supporting information; detailed methods are available in the supporting information). However, we did not consider impact melt clasts in the shape analysis because the sections that we investigated contained too few clasts to allow meaningful analysis. Detailed information for the designation and description of each clast type will be provided later in section 4. Grain contours were manually traced on four thin sections of the meteorite (Figures S1–S4). Grains that were on the border of a thin section were excluded from the analysis, since their shape might be affected by this position. The yellow, green, and magenta contours have different average resolutions on the images—i.e., a different number of pixels per grain contour—because of their different sizes. It is known that roundness, $R$, is affected by the number of pixels around the contour [*Manga et al*., 2011]. To allow comparison of contours among different grain populations, we reduced the resolution of images to the lowest observed value in the data set, 160 pixels per contour. This was accomplished by applying a bicubic resizing method to the images, where the output pixel value is a weighted average of pixels in the nearest $4 \times 4$ neighborhood (Figure S5).

In order to create naturally shaped rock fragments for comparison to the meteorite contours, we crushed limestone blocks with a hammer to generate fragments in the size range of $a = 15$–$35$ mm (Figure S5). After imaging the fragments on a high-contrast, rigid board, the image was thresholded and the resolution reduced to an average of 160 pixels per contour, as described above (Figure S5). We note that the image resolution for the fall-deposit pumice clasts was not reported in *Manga et al*. [2011]; however, it is likely larger than the average of 160 pixels per contour we applied. This may be one reason for the relative difference shown in Figure 2 between the values of the pumice clasts, and those associated with the limestone fragments and NWA 7034 clast contours.

Analyzing grains in a thin section requires some assumptions. Real particles are three-dimensional objects with axis lengths $a > b > c$. When plotting the axis ratio data in Figure 2, we assume that the three-dimensional grain contours we observe on the thin sections of the meteorite correspond to the $a$-$b$ plane of the three-dimensional grain. However, the orientation can be different, which may result in an underestimate of the axis lengths. An additional caveat in comparing data is that the contours of the limestone fragments and fall deposits are the maximum projection of three-dimensional grains, while the NWA 7034 clast contours are an arbitrary two-dimensional slice. While this difference is known to affect measured size and shape parameters [*Jutzeler et al*., 2012], their quantitative influence is not well understood at present. This factor likely introduces an additional, but unknown, error when comparing NWA 7034 data to other systems. The reasonable agreement of the NWA 7034 size-shape curve with terrestrial fragments (Figure 2), however, suggests that this error is small.

### 3.2. Expected Size Distribution for Fragments

The coarse tail of the meteorite size distribution can be well approximated by a power law with an exponent of $\gamma \approx 4$ (Figure 2). Brittle fracture theory predicts that the mass distribution of fragments should follow a power law decay with an exponent $\gamma = \frac{2D-1}{D}$, where $D$ is the dimensionality of the system [*Aström*, 2006; *Kekäläinen et al*., 2007]; for our three-dimensional case, $D = 3$. Since size scales as the one-third power of mass, we expect that the size distribution of fragments should exhibit $\gamma = 3\frac{2D-1}{D}$ [*Hartmann*, 1969], which translates to $\gamma = 5$. Terrestrial pyroclastic fall deposits usually show exponents smaller than this value; *Kaminski and Jaupart* [1998] report a range of $\gamma = 4.0$–$4.9$ from an extensive compilation of data. We note that their reported exponents are for the cumulative size distribution $N(a > r)r^{-}\beta$, where $N$ is the number of particles for which axis length $a$ is greater than $r$; the relationship between the exponents of their cumulative plots and our histogram is $\beta = \gamma - 1$ [*Hartmann*, 1969].

## 4. Results

### 4.1. Petrography of the Bulk Matrix of NWA 7034

NWA 7034 consists of a fine-grained interconnected groundmass that hosts a wide variety of clasts (Figures 1 and S1–S4). The interconnected groundmass that comprises NWA 7034 is referred to as the bulk-matrix

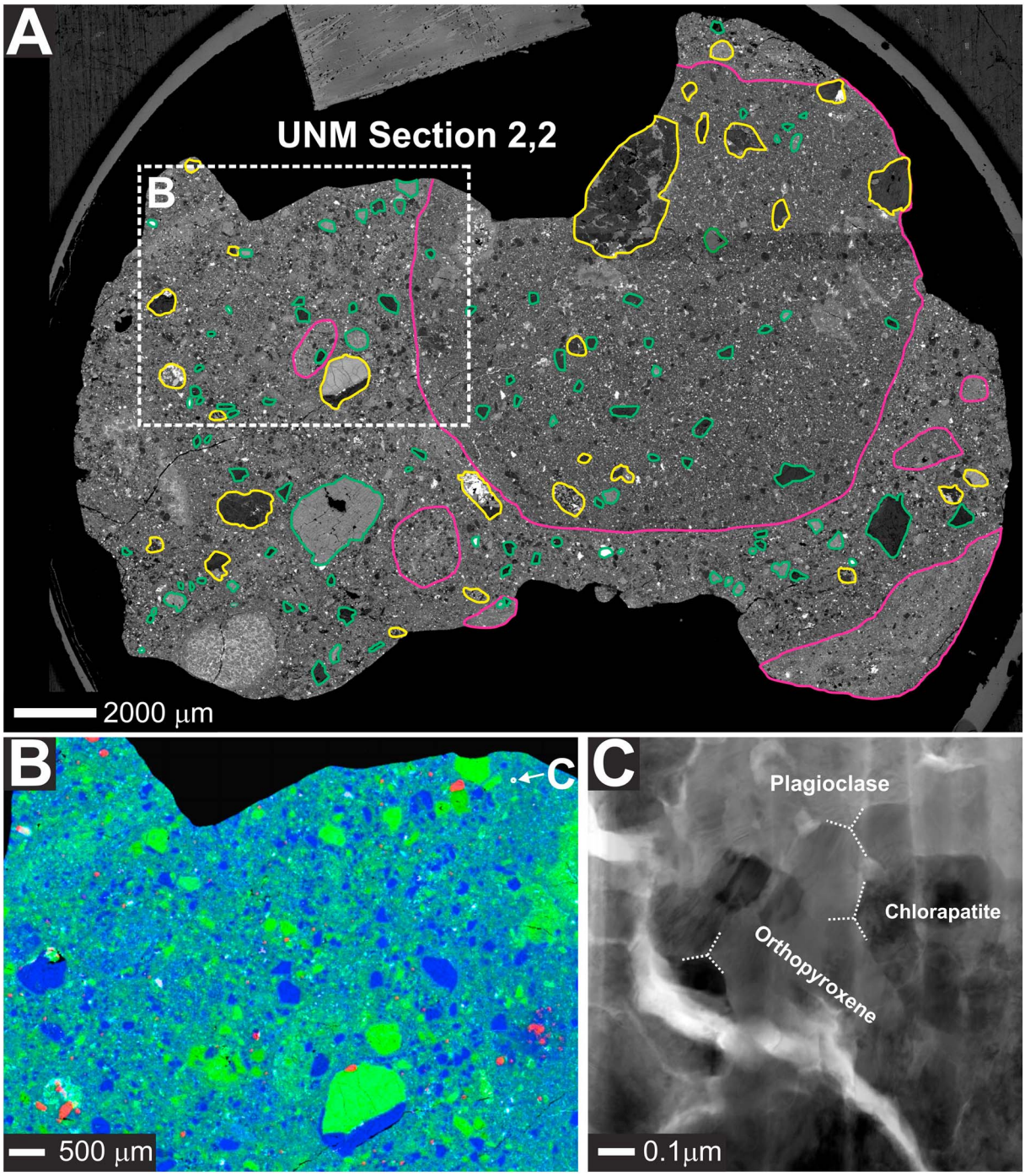


**Figure 1.** Images of various lithologic components in NWA 7034 from UNM thin section 2,2. a) Clast contours on a BSE image with clast contour colors indicating clast type as follows: the yellow outline presents the poly-phase igneous clasts that formed through crystallization of a magma or lava. The green outline presents the single mineral grains that were likely once part of a poly-phase igneous clast. The magenta outline presents the sedimentary clasts composed of either siltstone or sandstone. These clasts are also typically clast-bearing. A white dashed inset box indicates the field of view for Figure 1b. (b) RGB X-ray composite image with P = red, Mg = green, and Al = blue. The location of the FIB section extracted for TEM analysis in Figure 1c is indicated by a white circular outline. (c) TEM image of NWA 7034 groundmass. Minerals are labeled and some grain boundaries are outlined with a white dotted line.

domain [*Muttik et al.*, 2014; *Nyquist et al.*, 2016; *Santos et al.*, 2015] of the meteorite. Across the two FIB sections containing bulk matrix that we investigated, the materials studied in NWA 7034 are very similar to each other in terms of texture and mineralogy at the submicron scale. The bulk-matrix domain is composed of submicron- (0.1–1 μm) sized equigranular plagioclase, pyroxene, magnetite, ilmenite, and Cl-rich

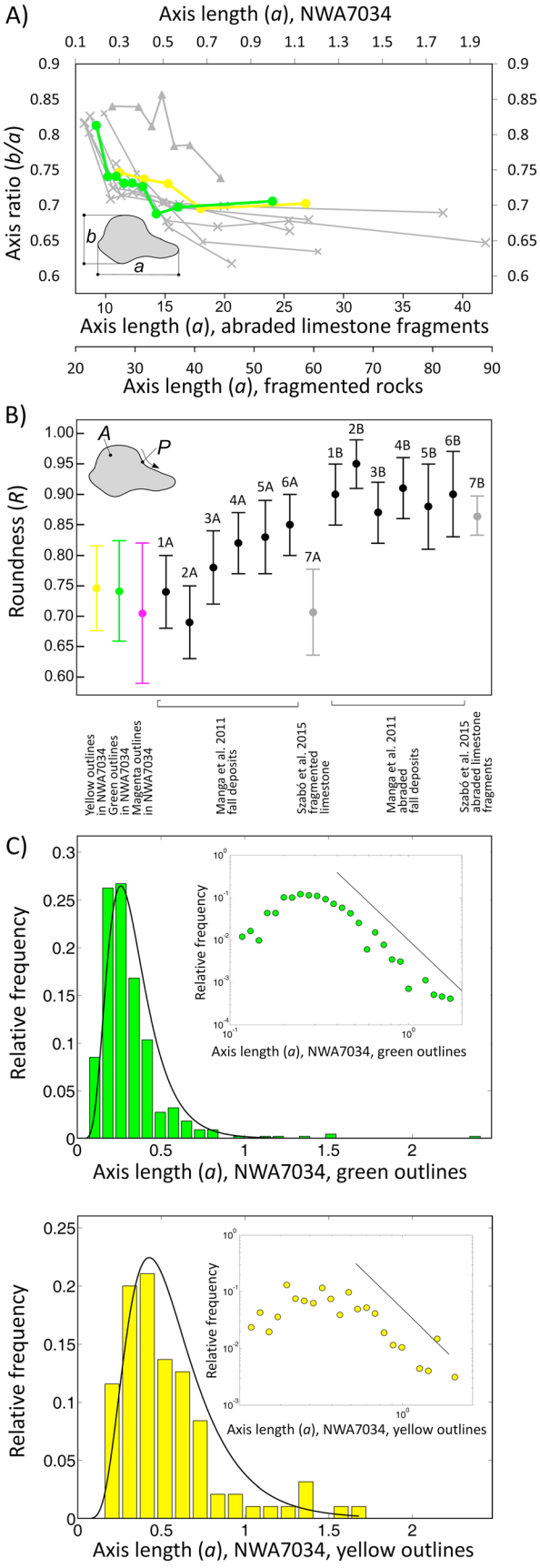


apatite grains that exhibit an interlocking texture and grain boundaries that commonly meet at 120° angles [e.g., *Muttik et al.*, 2014] (Figures 2 and 3). Several plagioclase and pyroxene grains are twinned (e.g., Figure 3i), and some of the matrix regions are locally enriched in pyrite (e.g., Figure 3h).

**Figure 2.** Shape and size data of grain contours in meteorite NWA 7034. Axis ratio *b/a* is the ratio of the smallest (*b*) to the longest (*a*) axis; roundness is defined as $R = 4\pi A/P^2$, where *A* is the area enclosed by the grain contour and *P* is the perimeter of the contour [*Blott and Pye*, 2008]. For a perfect circle $R = 1$, whereas for any other cross-sectional shape $R < 1$. (a) Relationship between *a* and *b/a* of igneous textured clasts (yellow outlines) and mineral clasts (green outlines) resemble the common relation found for fragmented rocks in *Domokos et al.* [2015] (gray data sets with x symbols). Well-rounded limestone clasts (gray data set with triangles, limestone fragments abraded in the laboratory from *Szabó et al.* [2015]) show a similar shape-size realationship but the curve is shifted upwards. (b) Mean ± standard deviation of *R* for igneous textured clast ($n = 95$), mineral clast ($n = 434$), and protobreccia clast ($n = 35$) outlines, as well as for fall-deposit pumice clasts from *Manga et al.* [2011] (black, 1A–6A) and for fragmented limestone clasts ($n = 81$) produced in the laboratory [*Szabó et al.*, 2015, blue, 7A,]. The pumice clasts originate from four volcanoes: 1A Mount St. Helens ($n = 20$), 2A Taupo ($n = 20$), 3A Lassen ($n = 20$), 4A Medicine Lake 12.5+ mm ($n = 40$), and 5A Medicine Lake 8–9.5 mm ($n = 40$), 6A Medicine Lake 12.5+ mm with 20% ash air fall ($n = 20$). 1A-2A fragments were mechanically created in the laboratory, while 4A-6A are fall-deposits (for details, see *Manga et al.* [2011]). Note that *R* depends on image resolution, which is identical (by design) for the Mars and limestone fragments but is higher for the *Manga et al.* [2011] data; thus, the relative differences between these data may be due to resolution. Well-rounded, abraded pumice (1B–6B [from *Manga et al.*, 2011]) and limestone clasts (7B [from *Szabó et al.*, 2015]) have a notably higher *R* value. (c) Size distribution of the green and yellow meteorite outlines with a fitted lognormal distribution with parameters $\mu = -1.158 = \ln(0.314\ \text{mm})$, $\sigma = 0.431 = \ln(1.539\ \text{mm})$ (green) and $\mu = -0.646 = \ln(0.524\ \text{mm})$, and $\sigma = 0.451 = \ln(1.569\ \text{mm})$ (yellow). Due to limited image resolution, only particles with $a > 0.1$ mm were outlined. Inset shows the size distribution on log-log scale with a reference power law slope of $\gamma = -4$, a common value for pyroclastic deposits (see text).

These textural properties are most consistent with a granoblastic texture. The magnetite is associated with maghemite in some cases [*Muttik et al*., 2014] (Figure 3). Additionally, high-resolution TEM images reveal minor phyllosilicate fringes with basal spacings measuring 10–11 Å consistent with saponite (a type of smectite) along the edges of some matrix pyroxene grain boundaries (Figure 3f), which was also observed by *Muttik et al*. [2014]. The bulk matrix is holocrystalline with no glass or amorphous phases. Olivine was absent from all of the bulk matrix portions of NWA 7034 analyzed in the present study.

### 4.2. Petrography of the Clasts Within NWA 7034

The clasts range in size from approximately 10 μm to greater than a centimeter in diameter (Figures 1 and S1–S4), and they are primarily composed of the same minerals that make up the bulk matrix domain, although there is also alkali-rich feldspar, zircon, baddeleyite, chromite, olivine (rare), pyrite, and merrillite (rare) in the clasts [*Leroux et al*., 2016; *Lorand et al*., 2015; *Santos et al*., 2015; *Shearer et al*., 2015; *Udry et al*., 2014]. Two broad categories of clasts are observed, characterized here as igneous or sedimentary in origin. The term igneous clast here is used broadly to include crystallization products from magmas, lavas, or impact melts. We do not attempt to distinguish further among these three possibilities in the present study. The term sedimentary clast here is used broadly to include any clasts that are composed of preexisting solid materials that have been plastered together and reconstituted into a coherent lithic mass that is distinct from the bulk matrix domain in NWA 7034. Importantly, this definition of sedimentary is inclusive of clastic rocks that have come together through bed load transport, pyroclastic processes, and/or impact processes. We will later use the results obtained in the present study to differentiate among these disparate processes.

The igneous clasts are composed of either a single mineral grain or a poly-phase assemblage. Petrographic descriptions of these clasts have been reported previously [*Humayun et al*., 2013; *Nyquist et al*., 2016; *Santos et al*., 2015; *Udry et al*., 2014; *Wittmann et al*., 2015], and our observations are similar to those reported in previous studies. The single mineral clasts include clinopyroxene, orthopyroxene, plagioclase, K-rich alkali feldspar, Ti-magnetite, chromite, ilmenite, zircon, baddeleyite, pyrite, Cl-rich apatite, and merrillite. The poly-phase igneous clasts are composed of either holocrystalline clasts exhibiting igneous textures or vitrophyric clasts that appear to be rapidly quenched partially crystallized melt products that exhibit highly rounded or amoeboid shapes [*Santos et al*., 2015; *Udry et al*., 2014]. The spherical shapes of many vitrophyric clasts indicate postquench deposition subsequent to formation by suspended transport resulting from impact or volcanic processes [*Wittmann et al*., 2015]. The amoeboid-shaped vitrophyric clasts, which are identical in texture and composition to the spherical vitrophyric clasts, were likely deposited in a partially molten state, which caused deformation during deposition [*Wittmann et al*., 2015]. In addition to the rare occurrence of olivine, the poly-phase igneous clasts are composed of the same mineralogy as the single-mineral clasts. Petrologic descriptions of all the poly-phase igneous clast types have been reported previously in great detail [*Agee et al*., 2013; *Bellucci et al*., 2015; *Humayun et al*., 2013; *Lorand et al*., 2015; *Nemchin et al*., 2014; *Nyquist et al*., 2016; *Santos et al*., 2015; *Udry et al*., 2014; *Wittmann et al*., 2015], so we will not duplicate those efforts here. However, one of the alkali basalt clasts (Clast 78) that was described by *Santos et al*. [2015] is investigated further in this study because it hosts zircon that is large enough for radiometric dating (smallest grain is approximately $20 \times 7$ μm; Figures S9e and S10). In addition, the previous studies have not described the submicron textures of the vitrophyric clasts, so we will report new results based on our FIB and TEM investigation to fully characterize the textures exhibited by the vitrophyric clasts and how they compare to other submicrometer domains within NWA 7034.

The sedimentary clasts are geochemically distinct from the interconnected groundmass of the NWA 7034 breccia (e.g., Figures 1 and S1–S4), although they are texturally similar. The sedimentary clasts have not been described in great detail previously, so we expand upon their descriptions here. The sedimentary clasts are best described as clastic lithologies, which were reported as siltstones in paired meteorite NWA 7475 [*Wittmann et al*., 2015]. *Wittmann et al*. [2015] identified two siltstone clasts, one coarse sand and one very coarse sand in size (0.9 and 1.4 mm, respectively) in NWA 7475 that are composed primarily of pyroxene fragments that are ~5 μm in size. In the present study, we have identified 53 of these sedimentary clasts in the four sections of NWA 7034 that we have examined (Figures S1–S4). The clasts can be distinguished from the bulk matrix domain based on their distinct textural and compositional features. Specifically, there is commonly a difference in clast distribution, and there are typically compositional differences that stand out in elemental X-ray images (Figures S1–S4). The sedimentary clasts are poorly sorted clastic materials

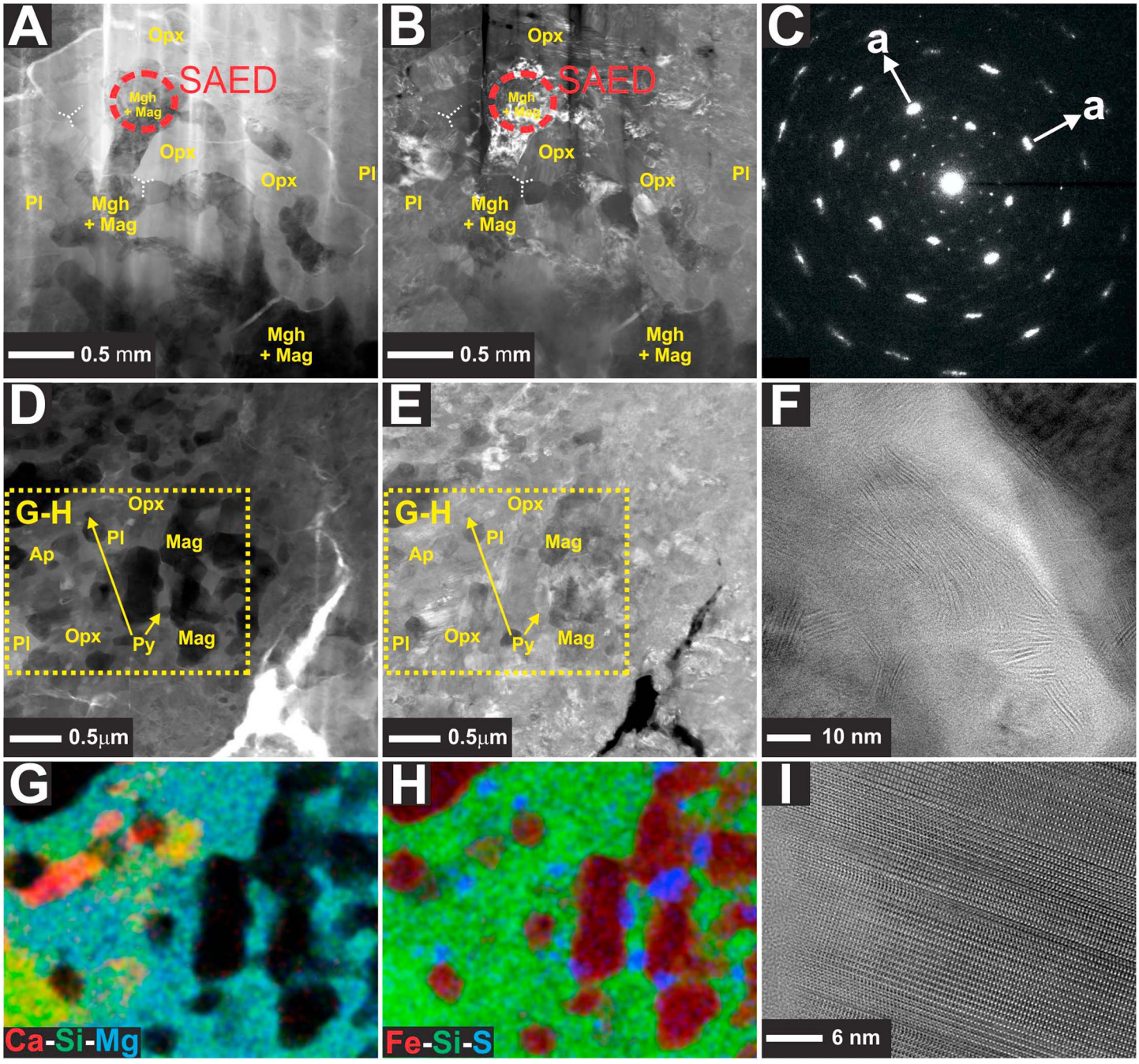


**Figure 3.** TEM results for the bulk matrix domain of NWA 7034. (a) Bright field image of region within bulk matrix domain in UNM thin section 3A,3 with phases identified as follows: Mag, magnetite; Mgh, maghemite; Opx, orthopyroxene; Pl, plagioclase. A region analyzed by selected area electron diffraction (SAED) is identified with a red-dashed circular outline. (b) Dark field image of same region as A with the same phases and features labeled. (c) SAED pattern of maghemite that exhibits the characteristic superstructure. *A* axis of magnetite is identified with white arrows. (d) Bright field image of pyrite-rich region within bulk matrix domain in UNM thin section 2,2 with phases identified as follows: Ap, apatite; Mag, magnetite; Opx, orthopyroxene; Pl, plagioclase; Py, pyrite. A region analyzed by energy dispersive X-ray (EDX) spectroscopy is identified with a yellow-dashed rectangular outline. (e) Dark field image of same region as Figure 3b with the same phases and features labeled. (f) High-Resolution TEM (HRTEM) image of saponite fringes along pyroxene grain boundaries in the bulk matrix domain with basal spacings of approximately ~1 nm. (g and h) EDX spectrometry maps from yellow-dashed region in Figures 3d and 3e displaying X-ray intensity of three elements overlaying each other. Red is Ca, Green is Si, and Blue is Mg (Figure 3g). Red is Fe, Green is Si, and Blue is S (Figure 3h). (i) HRTEM image of nano-twinned plagioclase within the bulk matrix domain.

that range in size from medium sand (smallest sedimentary clast is 380 μm in the longest dimension) to medium gravel (largest sedimentary clast is 13 mm in the longest dimension). We note here, however, that hand samples of NWA 7034 have some cobble-sized clasts that are texturally similar to the sedimentary clasts based on optical microscopic examination (Figure S6), but these clasts are not described in the present study. Additionally, there are sedimentary clasts that are equal to and smaller than the medium-sand-sized clasts; however, the resolution of our full section images used for clast identification and grain contouring (Figures S1–S4) limited identification of sedimentary clasts to larger than about 200 μm (i.e., Figure S7). Consistent identification of sedimentary clasts that are smaller than 200 μm would require targeted fine-scale X-ray mapping, which we considered to be beyond the scope of the present study. The sedimentary clasts are composed of lithic clasts and a submicron groundmass similar to the bulk-matrix domain in NWA 7034. Given that these clasts have both a matrix component and a clast component, we will describe each of these textural regimes independently. Furthermore, the sedimentary clasts appear to be previously lithified portions of Martian regolith, so, going forward, we refer to these sedimentary clasts as protobreccia clasts after previously established nomenclature [*Muttik et al*., 2014; *Nyquist et al*., 2016; *Santos et al*., 2015].

#### 4.2.1. Submicron Petrography of Vitrophyric Clasts

We identified a total of eight vitrophyric clasts in the four sections of NWA 7034 that we have examined (see the cyan clast outlines in Figures S1–S4), although they are reported in higher abundances in paired meteorite NWA 7475 [*Wittmann et al*., 2015]. *Udry et al*. [2014] described the mineralogy and geochemistry of a vitrophyric clast from NWA 7034, but they did not examine the clast at the submicron scale. We prepared a FIB section from the inner portion of one of the vitrophyric clasts that was embedded in the bulk matrix domain of NWA 7034 (Figure 4a) in order to gain an improved understanding of its texture and mineralogy. The textural characteristics of the extracted FIB section (Figures 4b–4h) are essentially identical to textures exhibited by the bulk matrix domain described above (Figures 4b and 4c); however, the mineralogy is distinct. The vitrophyric clast consists mostly of rounded to subhedral crystals of low-Ca pyroxene and plagioclase feldspar with heterogeneously distributed Fe-oxide phases. The silicate-rich portions of the clast exhibit the same granoblastic texture as those observed in the bulk matrix domain (Figure 4g). TEM images and electron diffraction patterns confirm that pyroxene and plagioclase grains are single crystals ranging in grain size from 100 nm to 1 μm. There is a heterogeneous distribution of Fe-oxide phases in the vitophyric clast compared to the bulk matrix domain. The vitrophyric clast has nanophase Fe-oxide (magnetite and maghemite) crystals with variable morphologies and textures embedded in pyroxene and plagioclase grains. In addition, ilmenite was interspersed with maghemite and magnetite (Figure 4h). The dominant Fe-oxide phases occur as well-crystallized, irregularly shaped crystals up to 1 μm in size. However, in addition to the rounded magnetite and maghemite phases, banded rims of maghemite surround the round crystals of magnetite (Figure 4d). In addition, we observed regions of fine-grained phyllosilicates along pyroxene grain boundaries. High-resolution TEM images show basal spacings measuring 10–11 Å, consistent with saponite. Despite the vitrophyric texture exhibited by the clast, we did not detect any glass or amorphous phases, indicating that the vitrophyre has been completely devitrified.

#### 4.2.2. Protobreccia Matrix

We examined the groundmass of the protobreccia clasts as well as the interface between protobreccia clasts and the bulk matrix domain by scanning electron microscopy as well as in three FIB sections (Figures 1 and 5). The protobreccia matrix is composed of fine-grained, crystalline mineral phases, similar in texture and mineralogy to the bulk matrix domain. The protobreccia clasts have a well-defined interface with the bulk matrix domain (Figures 5a–5e) that is discerned by coarser grain sizes of the matrix in the protobreccia clast as well as a lower abundance of Fe-oxides compared to the bulk matrix domain (Figure 5).

The protobreccia matrix is composed of variable amounts of Fe-Ti oxides embedded in a groundmass of plagioclase and pyroxene (Figure 5). Fe-Ti oxides are mainly magnetite and maghemite with less common occurrences of ilmenite. Chlorine-rich apatites are present as rounded, subhedral crystals that are approximately 300 nm in size. The protobreccia matrix exhibits a granoblastic texture, with interlocking grain boundaries at 120°. The pyroxenes in the protobreccia matrix range in grain size from 100 nm to 2 μm and plagioclase grain sizes range from 100 nm to several μm (Figures 5f–5i). Consequently, the average grain sizes of the protobreccia matrix are larger than the bulk matrix domain (Figures 3 and 5). Plagioclase is the primary feldspar, and there are minor occurrences of phyllosilicates, comparable to the saponite that was reported in the vitrophyric clast.

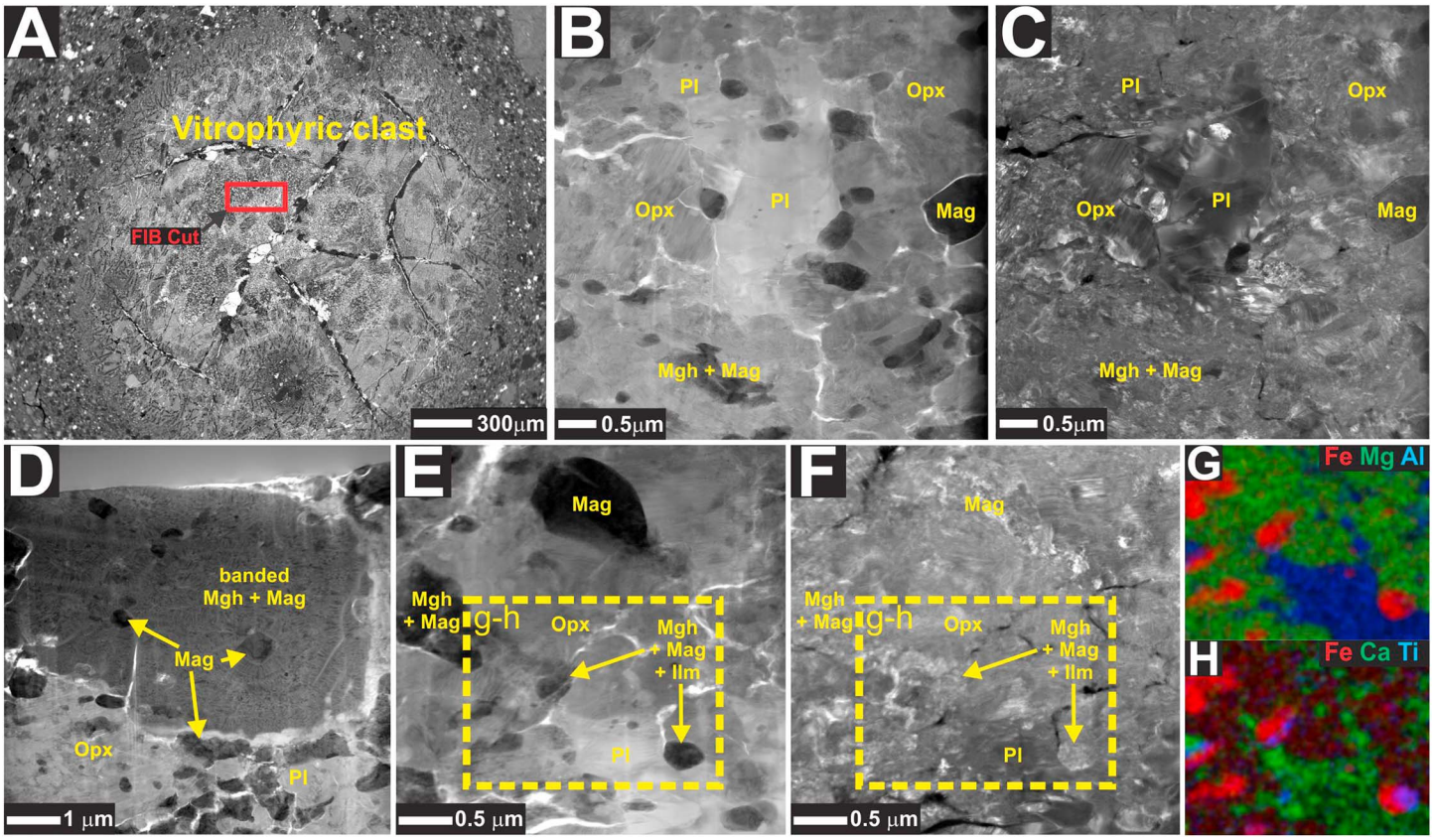


**Figure 4.** Images of a large vitrophyric clast from NWA 7034 UNM thin section 3A,3. (a) BSE image of the vitrophyric clast, which is labeled with yellow text. A red rectangular outline denotes the region from which a FIB section was extracted for analysis by TEM. (b) Bright field image of region within the vitrophyric clast with phases identified as follows: Magm magnetite, Mgh, maghemite, Opx, orthopyroxene, Pl, plagioclase. (c) Dark field image of same region as b with the same phases labeled. (d) Bright field image of oxide-rich region within the vitrophyric clast with phases identified as follows: Mag, magnetite; Mgh maghemite; Opx, orthopyroxene; Pl, plagioclase. The region of banded magnetite and maghemite is labeled on the image. (e) Bright field image of region within the vitrophyric clast with phases identified as follows: Ilm, ilmenite; Mag, magnetite; Mgh, maghemite; Opx, orthopyroxene; Pl, plagioclase. A region analyzed by energy dispersive X-ray (EDX) spectroscopy is identified with a yellow-dashed rectangular outline. (f) Dark field image of same region as b with the same phases and features labeled. (g and h) EDX spectrometry maps from yellow-dashed region in Figures 4e and 4f displaying X-ray intensity of three elements overlaying each other. Red is Fe, green is Mg, and blue is Al (Figure 4g). Red is Fe, green is Ca, and blue is Ti (Figure 4h).

In addition to the groundmass and clasts, one of the large protobreccia clasts hosts veins of Fe-oxides that crosscut clasts and matrix and terminate at or before the interface between the protobreccia clast and bulk matrix domain (Figures 5 and 6). These veins are approximately 1–10 μm wide and up to several millimeter in length (Figure 6). They are composed primarily of magnetite, with minor amounts of Cr, Mg, and Ti as determined by SAED and energy-dispersive analysis of X-rays, respectively (Figure 6). These veins can be traced to altered mineral clasts within the protobreccia clasts, where Fe-oxides have partially replaced pyroxenes (Figures 5 and 6). Additionally, some of the veins can be traced to pyrite-rich domains within the protobreccia clast, where pyrite is hosted by pyroxene (Figures 6–8) and pyrite cores are surrounded by banded rims of magnetite and maghemite (Figures 7 and 8). Pyrite, magnetite, and maghemite were each identified by both SAED and Raman spectroscopy (Figures 7 and 8). These secondary alteration textures are not present within the bulk matrix domain within the sections of NWA 7034 that we have examined, although altered clasts of pyrite without associated magnetite veins do occur within the bulk matrix domain [*Lorand et al*., 2015; *Muttik et al*., 2014] (Figure 8). In total, we identified 23 distinct sites within seven protobreccia clasts that exhibit evidence of secondary alteration. These regions are outlined in orange in Figures S1–S4.

#### 4.2.3. Clasts Within Protobreccia Clasts

The clasts within the protobreccia clasts typically exhibit silt-sized to fine sand-sized grain sizes, although the protobreccia clasts host clast sizes that range from silt to very fine gravel. However, given the preponderance of clast sizes in the silt and sand size range, the protobreccia clasts in NWA 7034 are characterized as poorly

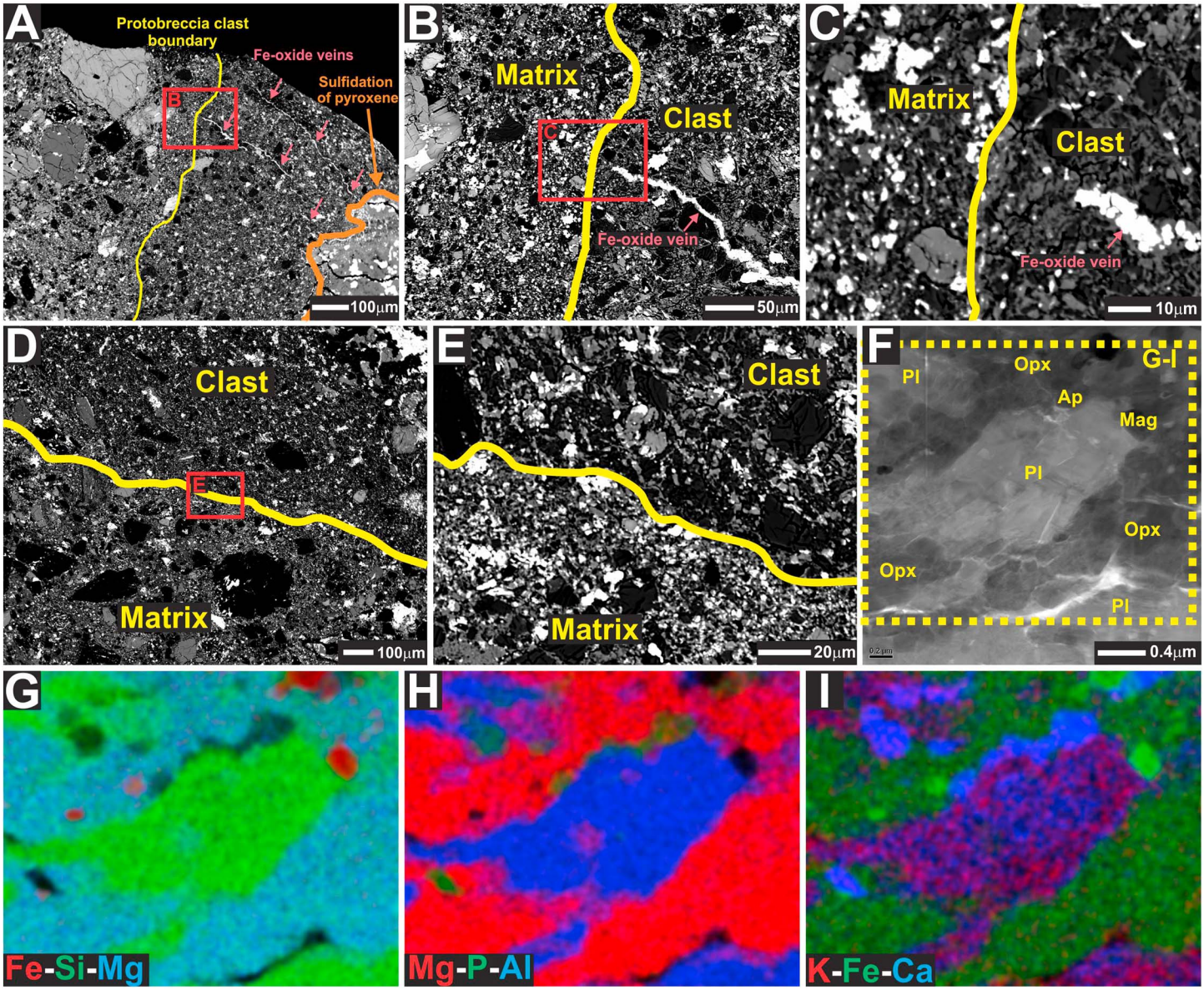


**Figure 5.** Images of the large protobreccia clast matrix in UNM thin section 2,2 as well as the interface between the bulk matrix domain and the large protobreccia clast. The clast boundaries are separated by a solid yellow line and the bulk matrix domain and protobreccia clast portions of the images are labeled with the terms matrix and clast, respectively). (a) Low-magnification BSE image of the boundary between the bulk matrix domain and the protobreccia clast. A sulfide-rich region within the protobreccia clast is outlined with a solid orange line and identified with orange text. Fe oxide veins within the protobreccia clast are identified with pink arrows. (B) Medium-magnification BSE image of the boundary between the bulk matrix domain and the protobreccia clast. A solid red-outlined rectangle in Figure 5a denotes the field of view for Figure 5b. Fe oxide vein within the protobreccia clast is identified with a pink arrow. (c) High-magnification BSE image of the boundary between the bulk matrix domain and the protobreccia clast. Fe oxide vein within the protobreccia clast is identified with a pink arrow. A solid red-outlined rectangle in Figure 5b denotes the field of view for Figure 5c. (d) Low-magnification BSE image of the boundary between the bulk matrix domain and the protobreccia clast. (e) High-magnification BSE image of the boundary between the bulk matrix domain and the protobreccia clast. A solid red-outlined rectangle in Figure 5d denotes the field of view for Figure 5e. (f) Bright field image of region within the large protobreccia clast with phases identified as follows: Ap, apatite; Mag, magnetite; Opx, orthopyroxene; Pl, plagioclase. A region analyzed by EDX spectroscopy is identified with a yellow-dashed rectangular outline. (g–i) EDX spectrometry maps from yellow-dashed region in Figure 5f displaying X-ray intensity of three elements overlaying each other. Red is Fe, green is Si, and blue is Mg (Figure 5g). Red is Mg, green is P, and blue is Al (Figure 5h). Red is K, green is Fe, and blue is Ca (Figure 5i).

sorted siltstones and sandstones (i.e., silt clasts range from 3.9 to 62.5 μm in size and sand clasts range from 62.5 μm to 2 mm in size), similar to the two siltstone clasts reported by *Wittmann et al.* [2015]. The sand and silt-sized clasts within the protobreccia clasts are composed of either single mineral grains or poly-phase assemblages, similar to the clasts that occur within the bulk matrix domain of NWA 7034. The mineralogy

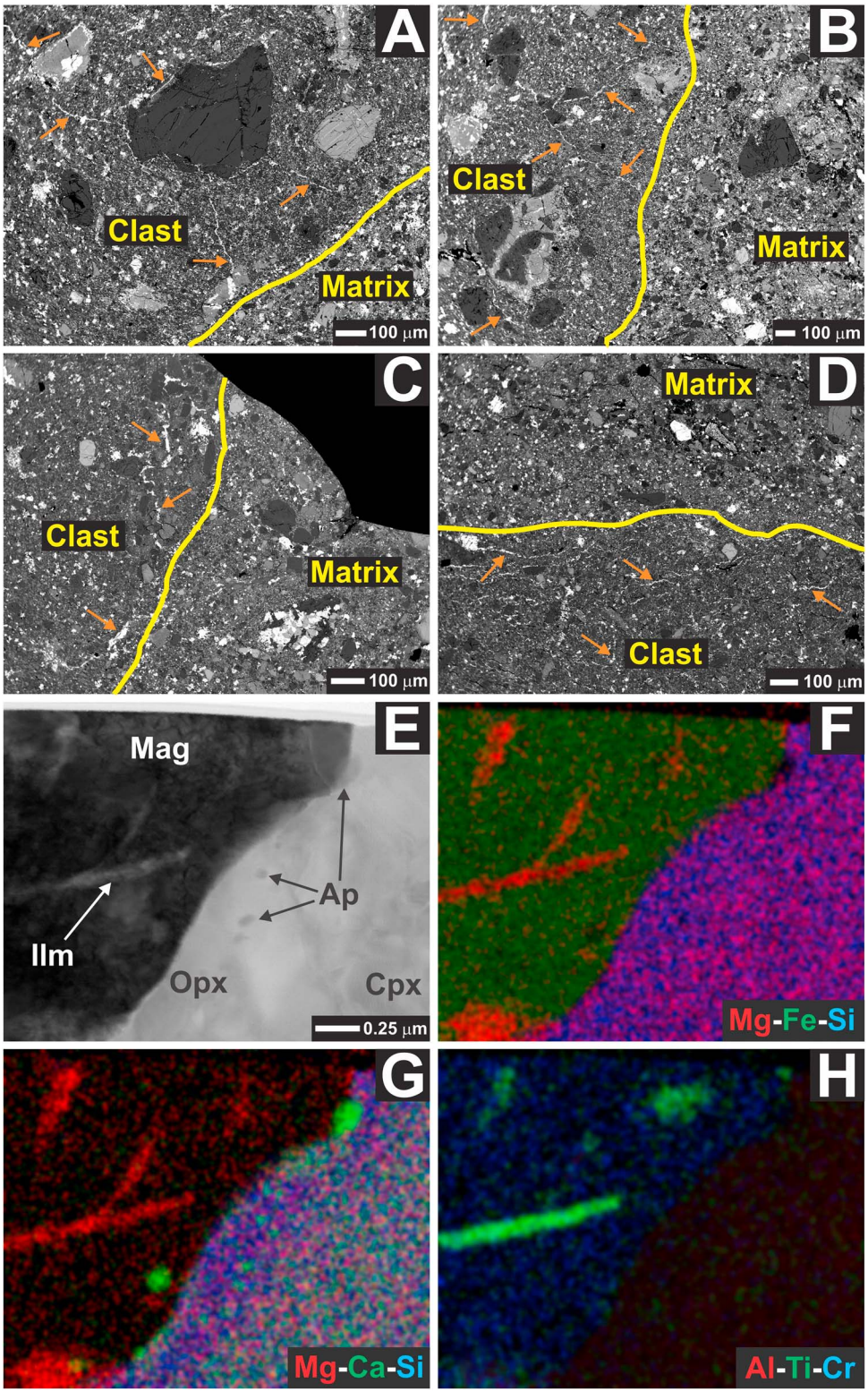


**Figure 6.** Images of Fe-oxide veins in the large protobreccia clast in NWA 7034 UNM thin section 2,2. (a–d) BSE images of four different interfaces between the bulk matrix domain and protobreccia clast. The clast boundaries are demarcated by a solid yellow line, and the bulk matrix domain and protobreccia clast portions of the images are labeled with the terms matrix and clast, respectively. Fe oxide veins are identified with an orange arrow. (e) Bright field image of region within the large protobreccia clast with phases identified as follows: Ap, apatite, Cpx, clinopyroxene; Ilm, ilmenite; Mag, magnetite; Opx, orthopyroxene. (f–h) EDX spectrometry maps from E displaying X-ray intensity of three elements overlaying each other. Red is Mg, green is Fe, and blue is Si (Figure 6f). Red is Mg, green is Ca, and blue is Si (Figure 6g). Red is Al, green is Ti, and blue is Cr (Figure 6h).

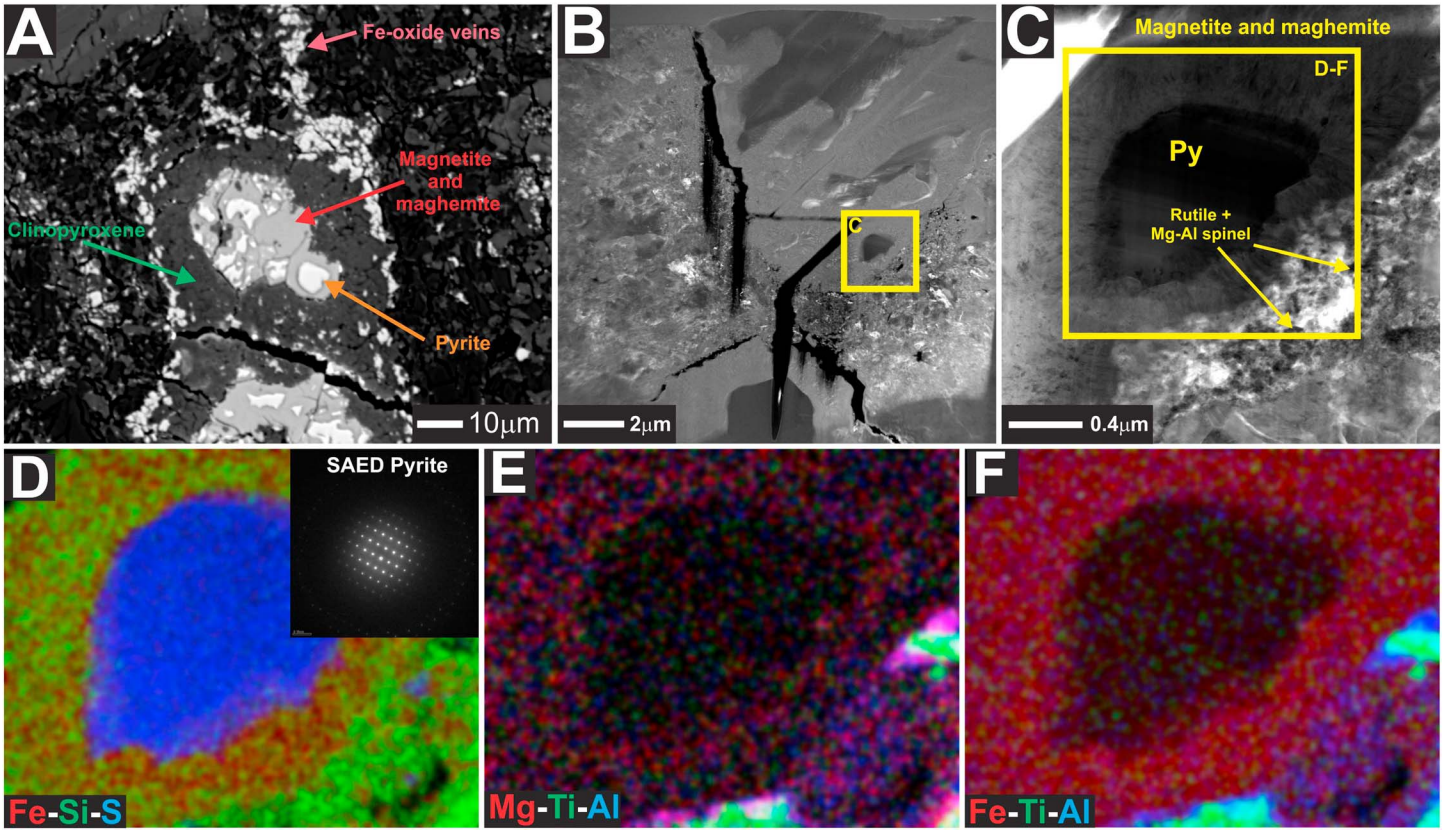


**Figure 7.** Images of pyrite-rich regions within the large protobreccia clast in NWA 7034 UNM thin section 2,2. (a) BSE image of pyrite (orange arrow), magnetite (red arrow), and maghemite (red arrow) within a clinopyroxene (green arrow). An Fe-oxide vein stemming from this region is labeled with a pink arrow. (b) Darkfield STEM image with phases labeled. (c) Bright field STEM image with phases labeled. A yellow inset box in Figure 5b shows the area represented by the TEM images in Figure 7c. (d–f) Energy dispersive X-ray spectrometry maps from yellow outlined region in Figure 7c displaying X-ray intensity maps of three elements overlaying each other. Red is Fe, green is Si, and blue is S (Figure 7d). Inset image shows an SAED pattern of the pyrite grain. Red is Mg, green is Ti, and blue is Al (Figure 7e). Red is Fe, green is Ti, and blue is Al (Figure 7f).

and petrology of the clasts are also very similar to those in the bulk matrix domain [*Humayun et al.*, 2013; *Nyquist et al.*, 2016; *Santos et al.*, 2015; *Udry et al.*, 2014; *Wittmann et al.*, 2015]; however, there is a higher concentration of zircons and K-rich alkali feldspar clasts in the large protobreccia clast in NWA 7034 section 2,2 in comparison to the clast population in the bulk matrix domain of NWA 7034 as determined by electron backscatter diffraction (EBSD) mapping and X-ray mapping of potassium, respectively (Figure 9). Additionally, some of the mineral clasts in the protobreccia clasts exhibit evidence of secondary alteration based on apparent partial replacements by pyrite and magnetite (Figures 6 and 7).

### 4.3. Grain-Shape Analysis

To constrain the depositional processes that created the bulk NWA 7034 breccia, we analyzed the shape and the size distributions for three particle classes that were identified based on compositional and textural differences: igneous textured clasts (yellow clast outlines; $n = 95$), monomineralic igneous clasts (green clast outlines; $n = 434$), and protobreccia clasts (magenta clast outlines; $n = 35$) (Figures 1 and S1–S4; detailed methods are available in the supporting information). We did not consider impact melt clasts in the shape analysis because the sections that we investigated contained too few clasts to allow meaningful analysis. Furthermore, we did not consider any clasts whose boundaries intersected the edge of the thin section. We choose the longest axis length, $a$, to represent particle size. Only particles with $a > 0.1$ mm were measured due to limited image resolution. To characterize shape, we consider two commonly used parameters: (1) the "axis ratio" (shortest ($b$) over longest ($a$)) and (2) roundness ($R$) (Figure 2). Mean size and shape parameters were computed for all three clast types considered (green, yellow, and magenta); however, full distributions are only presented for the yellow and green grain contours for which sample size ($n = 95$ and 434,

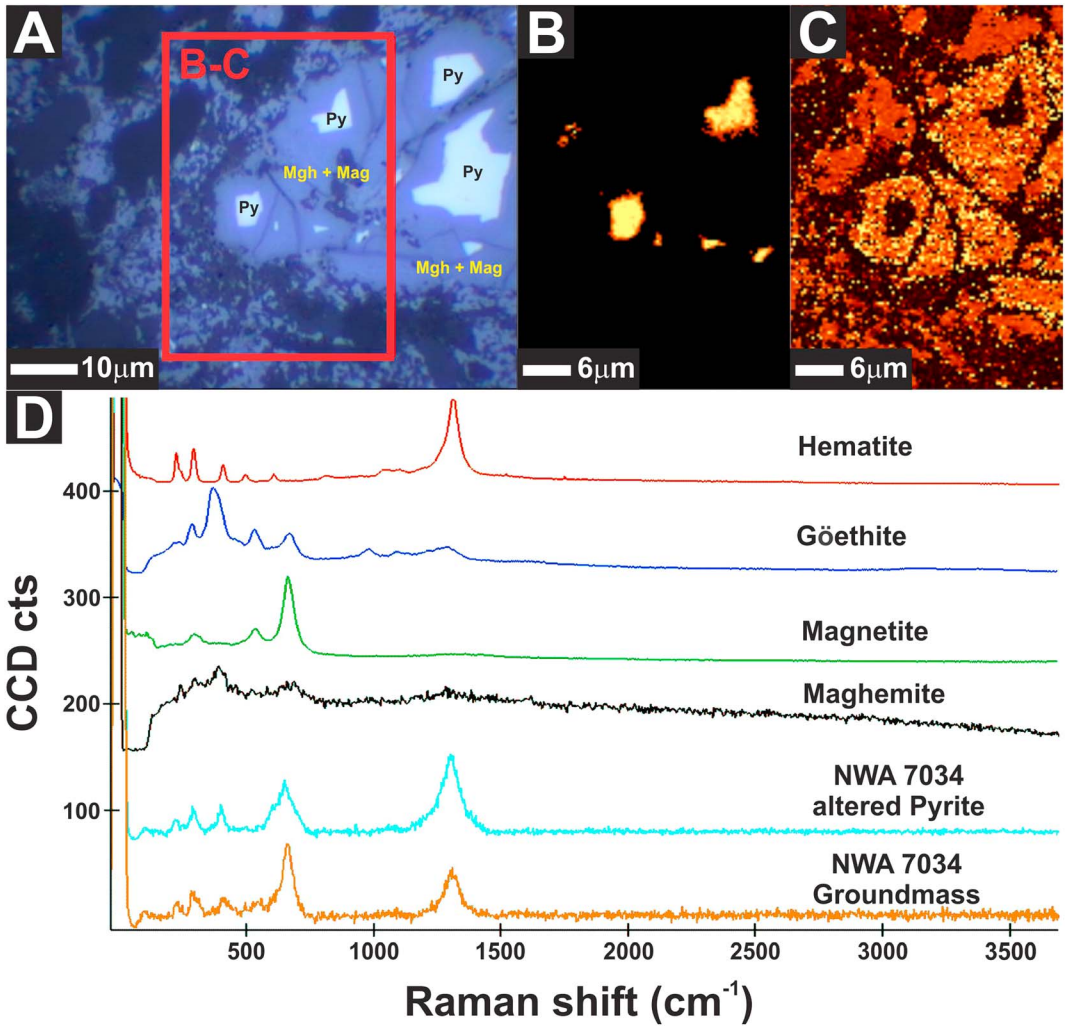


**Figure 8.** Altered pyrite clast within bulk matrix domain of NWA 7034 section 3A,2. (a) Reflected light image of pyrite and oxide assemblage: A red inset box shows the field of view for Figures 8b and 8c. (b) Raman spectral image showing location of pyrite. (c) Raman multispectral image showing location of Fe-oxides. (d) Raman spectra of several known Fe-oxides compared to two Raman spectra of NWA 7034.

respectively) was sufficient to analyze distributions. The first important result is that the axis ratio (for yellow and green clasts) decreases systematically with increasing particle size. This trend shows a good quantitative match with the common relation observed for freshly fragmented rocks (Figure 2a) [*Domokos et al*., 2015]. Second, in Figure 2b we find that both the average roundness and its standard deviation are equal to or lower than reported values for volcanic pumice fall-deposits [*Manga et al*., 2011] and also freshly broken limestone fragments created in the laboratory [*Szabó et al*., 2015] (Figure S5). Since roundness of initially angular particles is known to increase rapidly under the action of abrasion [*Domokos et al*., 2014; *Manga et al*., 2011; *Szabó et al*., 2015] (see 1B–7B in Figure 2b), we conclude that the lithic clasts are fragments that have not experienced significant collisions due to sediment transport.

Particle sizes range from the minimum resolvable value, $a = 0.1$ mm, up to a few millimeters for the protobreccia clasts (magenta). Mean particle sizes vary slightly among different classes, but they are all in the medium/coarse sand range (0.25–2 mm) with mean ± standard deviation values as follows: 0.58 ± 0.31 mm for the igneous textured clasts (yellow), 0.35 ± 0.20 mm for the monomineralic igneous clasts (green), and 1.21 ± 0.89 mm for the protobreccia clasts (magenta). Particles are poorly sorted by size compared to terrestrial fluvial and aeolian deposits [*Friedman*, 1962; *Jerolmack et al*., 2011]. As is observed for virtually all sedimentary deposits (e.g., fluvial [*Friedman*, 1962]), particle size histograms are reasonably well fit by a

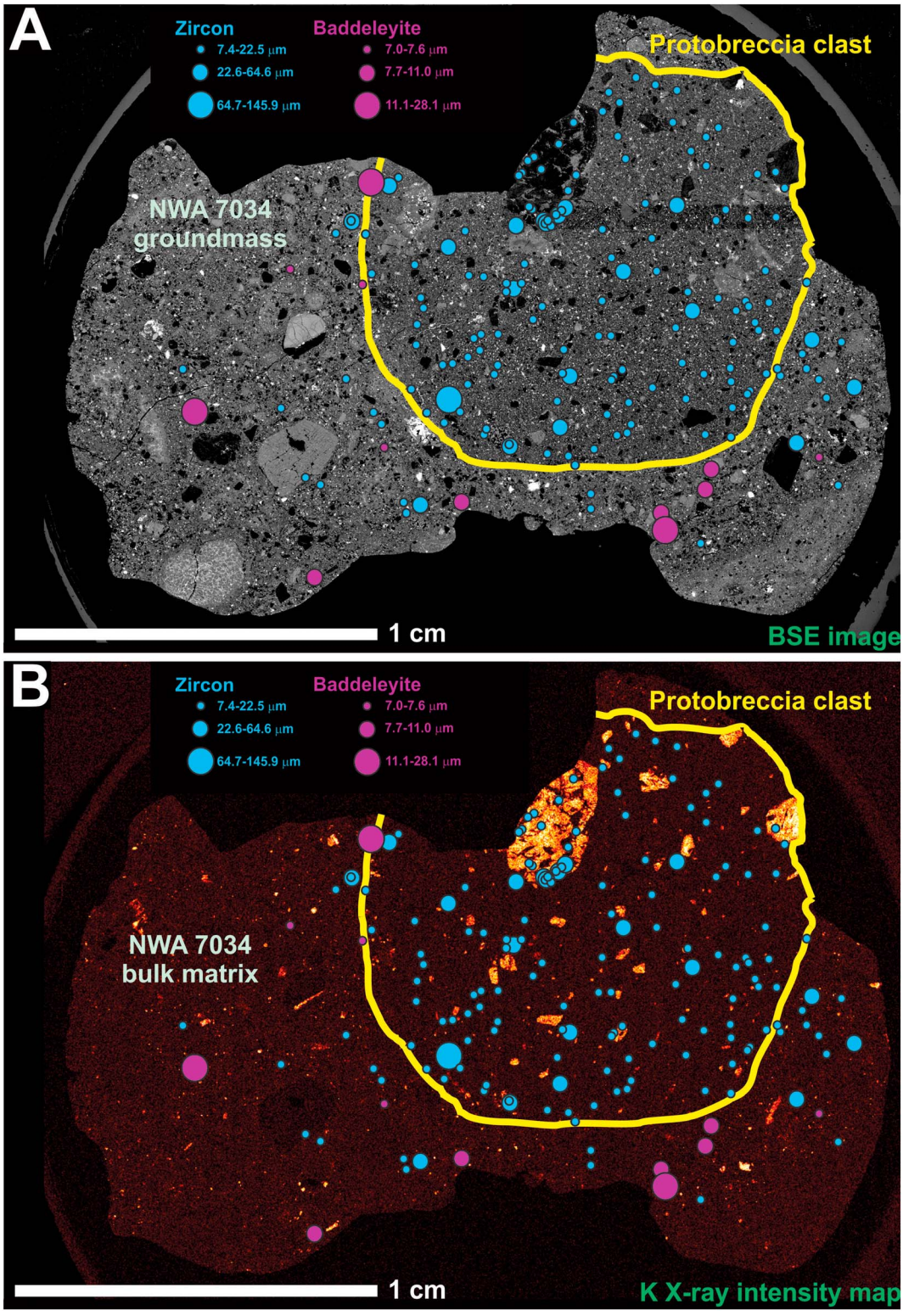


**Figure 9.** Map of the distribution of Zr-rich phases across NWA 7034 UNM thin section 2,2. Protobreccia clast outlined in yellow and NWA 7034 groundmass labeled with light green. Zircons and baddeleyite were identified by EBSD mapping of the thin section and are indicated by blue or purple spheres respectively. The diameter of the sphere correlates to the grain size of the Zr-bearing phase according to the legend. (a) BSE mosaic. (b) Potassium X-ray intensity mosaic.

lognormal distribution (Figure 2c). This distribution is known to underfit the tails of most natural deposits, however, which show power law behavior with slopes that are sensitive to transport history [*Bagnold*, 1941; *Jerolmack et al*., 2011]. The fine tail cannot be assessed with our data given the size cutoff at $a = 0.1$ mm, and the monomineralic igneous clasts (green) are the only particle class with a sufficient sample size to assess the coarse tail. Its particle size histogram indicates that for $a > 0.5$ mm, the data approximate a power law decay with an exponent of approximately $\gamma = 4$ (Figure 2c). Theory predicts an exponent $\gamma = 5$ for particles produced by fragmentation [*Aström*, 2006; *Kekäläinen et al*., 2007]; however, fragmentation in nature is often "incomplete," and therefore, the exponent rarely reaches this steady state limit [*Kaminski and Jaupart*, 1998].

### 4.4. Geochronology

A subset of the mineral clasts within NWA 7034 can be utilized to determine age information using the U-Pb geochronological system, including zircon, baddeleyite, and apatite. We identified zircon and baddeleyite within the NWA 7034 bulk matrix domain, as well as zircon grains within one of the medium-gravel-sized protobreccia clasts for subsequent analysis (Figures S8–S10). We performed Pb-Pb and U-Pb geochronology in the Zr-rich phases by secondary ion mass spectrometry (SIMS) using a NanoSIMS 50 and a SHRIMP-RG. We also examined the U-Pb systematics (Table S7) and trace element chemistry (Table S8) of Cl-rich apatite by SIMS with a SHRIMP-RG (U-Pb) within several petrographic domains in NWA 7034, including the bulk matrix domain, the medium-gravel-sized protobreccia clast, basaltic clasts, FTP clasts (igneous clasts rich in Fe, Ti, and P [*Santos et al*., 2015]), and a vitrophyric clast (Figures S12–S15).

#### 4.4.1. SHRIMP-RG U-Pb Dating, NanoSIMS U-Pb Dating, and Chemical Analysis of Zircon

A total of three zircon grains were analyzed by SHRIMP-RG for U-Pb dating, and seven grains were analyzed by SHRIMP-RG for trace elements. A total of six zircon grains were analyzed by Nano-SIMS for U-Pb dating, and nine grains were analyzed for major and minor elements by EPMA. Of the grains that were measured for U-Pb dating, two (Zircon 1 and Zircon 4) were measured both by SHRIMP-RG and NanoSIMS. Five of the zircons analyzed for U-Pb dating are crystal clasts that reside in the medium-gravel-sized protobreccia clast (Figure S8), one zircon is hosted by a basaltic igneous clast (Clast 78 from *Santos et al*. [2015]) within the medium-gravel-sized protobreccia clast (Figure 10), and one zircon grain is a crystal clast that resides within the bulk matrix domain (Figures S8–S10). Abundances of $HfO_2$ (0.76–1.94 wt %; Table S1) and $Fe_2O_3$ (0.13–3.36 wt %; Table S1) were determined for all zircons by using EPMA. The U and Th abundances of the zircon varied widely from 9 ppm to 2780 ppm U and from 7 ppm to 8580 ppm Th (Table S4). All of the zircon REE patterns were heavy rare earth element-enriched with La/Yb values ranging from 0.0004 to 0.14, although the higher portion of this range could be skewed due to ion beam overlap with other phases as evidenced by elevated alkali abundances (Table S4). Interestingly, Zircon 1 and Zircon 3 have more than 1 wt % $K_2O$, which cannot be explained by beam overlap, indicating substantial secondary alteration, possibly related to hydrothermal alteration subsequent to radiation damage.

The U-Pb data from all of the zircons analyzed in the present study exhibited a bimodal distribution in ages. The older zircons were plotted on Wetherill concordia diagrams and yielded a concordant date of 4.43 ± 0.03 Ga (Figure 11a), and the younger zircons yielded a concordant date of 1.50 ± 0.10 Ga (Figure 11b). Several U-rich zircon grains (Tables S2 and S3) yielded concordant ages of approximately 1.4–1.5 Ga (Figure 11b), while others plotted along a discordia line with an upper intercept at approximately 4.4 Ga and a lower intercept at around 1 Ga (Figure 11a). The bimodal distribution in ages correlated quite strongly with the U abundance of the zircon grains (Figure S11), which was also observed previously by *Humayun et al*. [2013]. We investigated the crystallinity of several zircons analyzed in our study (i.e., Zircon 1, Zircon 2, and Zircon 4), and we determined that both of the young, U-rich zircons are presently amorphous, indicating that they have been metamictized (Tables S2 and S3). Furthermore, the old, U-poor zircon remains crystalline (Tables S2 and S3).

#### 4.4.2. NanoSIMS Pb-Pb Dating and Chemical Analysis of Baddeleyite

Two baddeleyite grains were analyzed by NanoSIMS, and both grains were individual subhedral to anhedral crystal clasts within the bulk matrix domain (Figures S8 and S9). Although baddeleyite is primarily composed of $ZrO_2$, it is known to have trace and minor abundances of other elements. Concentrations of Ti, Fe, and Hf were measured by using EPMA, and the U and Pb concentrations were measured with NanoSIMS. Based on the EPMA results, Baddeleyite 1 has 1.58–1.70 wt % $HfO_2$, 0.93–1.29 wt % $Fe_2O_3$, and 0.53–0.57 wt % $TiO_2$ and Baddeleyite 2 has 2.01–2.60 wt % $HfO_2$, 0.74 wt % $Fe_2O_3$, and 0.51–0.53 wt % $TiO_2$ (Table S1). Three NanoSIMS

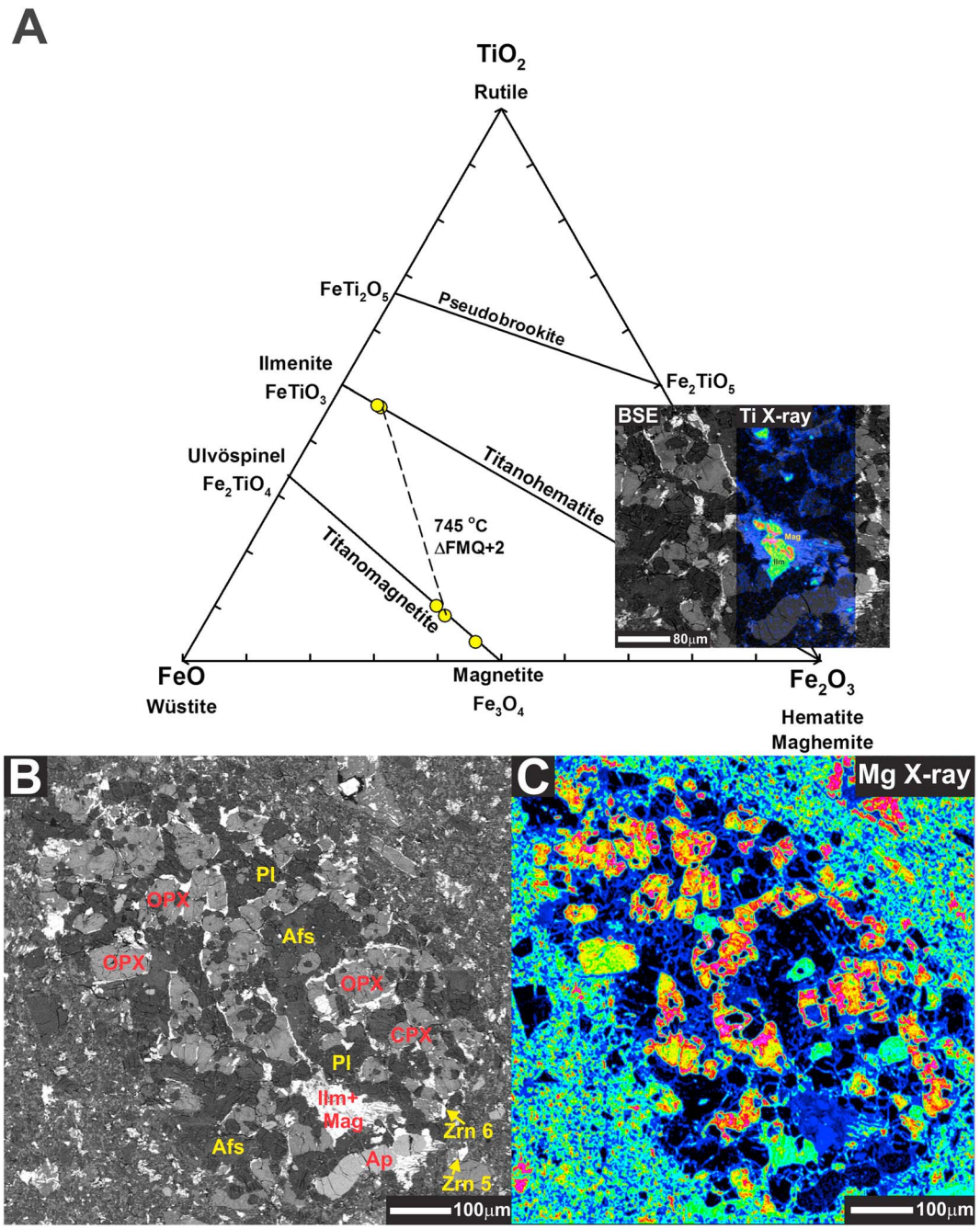


**Figure 10.** Zircon-hosting alkali basalt clast (Clast 78 from *Santos et al.* [2015]) that occurs in the large protobreccia clast in NWA 7034 UNM section 2,2. (a) FeO-$TiO_2$-$Fe_2O_3$ ternary showing the Fe-Ti oxide compositions in Clast 78 as yellow points. A dashed black tie line connects and Fe-Ti oxide pair that appears to be in equilibrium based on the distributions of Mg and Mn [i.e., *Bacon and Hirschmann*, 1988]. The temperature and $fO_2$ of equilibration for the equilibrium Fe-Ti oxide pair were estimated by using the program QUILF [*Andersen et al.*, 1993]. An inset box displays a BSE image with a partial overlay of a Ti X-ray intensity map indicating the texture of the Fe-Ti oxides in Clast 78. (b) BSE image of Clast 78 and surrounding protobreccia matrix with phases labeled as follows: Afs, alkali feldspar; Ap, apatite; CPX, clinopyroxene; Ilm, ilmenite; Mag, magnetite; OPX, orthopyroxene; Pl, plagioclase; Zrn, zircon. (c) Mg X-ray intensity map of Clast 78 and surrounding protobreccia matrix.

analyses of Baddeleyite 1 ranged in U abundance from 446 to 732 ppm and in Pb abundance from 341 to 484 ppm (Table S5), while two analyses of Baddeleyite 2 yielded 121–154 ppm U and 37–93 ppm Pb (Table S5). Although their dates represent minimum ages, both grains yielded consistent $^{207}Pb/^{206}Pb$ average dates of 4.38 ± 0.06 Ga and 4.30 ± 0.08 Ga for Baddeleyites 1 and 2, respectively (Table S5).

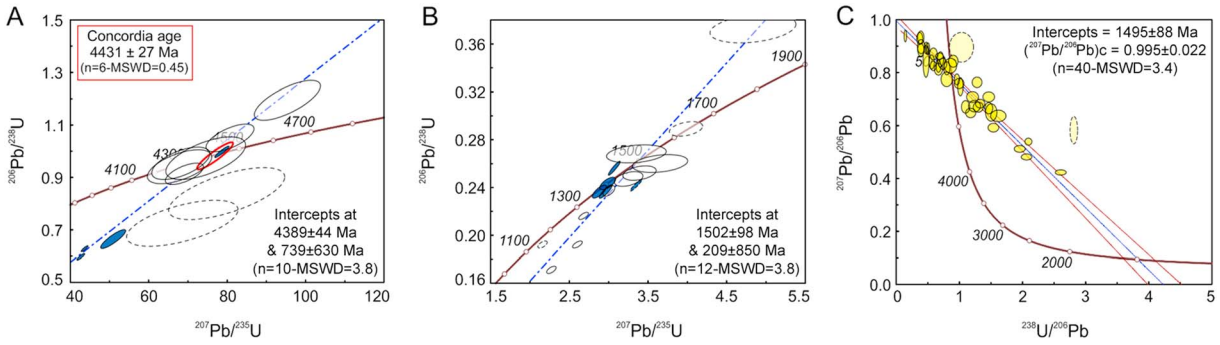


**Figure 11.** U-Pb dating results. (a) Wetherill concordia diagram showing results for NWA 7034 "old" zircons from SHRIMP-RG (blue ellipses) and NanoSIMS (white ellipses) analyses. Concordia date (red ellipse) is from weighted mean of concordant NanoSIMS and SHRIMP-RG data. The dashed ellipses are excluded as outliers. Upper and lower concordia intercept dates are calculated by using unweighted regressions due to the relatively high MSWD values and variable uncertainties of the data. The high MSWD values reflect excess scatter that we interpret to reflect real geologic complexity. Importantly, the uncertainties on our final dates reflect this degree of scatter in addition to the a priori errors simply based on counting statistics. (b) Wetherill concordia diagram showing results for NWA 7034 "young" zircons from SHRIMP-RG (blue ellipses) and NanoSIMS (white ellipses) analyses. (c) Tera-Wasserburg concordia diagram showing results for NWA 7034 Cl-apatite obtained with the SHRIMP-RG. In all the plots error ellipses are 1 sigma uncertainties; when dates are calculated uncertainties are given at 95% confidence (2 sigma); the dashed ellipses are not included in date calculations.

#### 4.4.3. SHRIMP-RG U-Pb Dating and Chemical Analysis of Apatite

A total of 17 apatite grains were analyzed by SHRIMP-RG for U-Pb dating across several petrographic domains, including the bulk matrix domain, the medium-gravel-sized protobreccia clast, basaltic clasts, FTP clasts (igneous clasts rich in Fe, Ti, and P [*Santos et al*., 2015]), and a vitrophyric clast (Figures S12–S15). The apatites are subhedral to anhedral in shape, and they are all Cl-rich apatite, as determined by EPMA (Table S6). The apatites analyzed in the present study have Cl abundances ranging from 3.42 to 5.31 wt % and F abundances ranging from 0.51 to 1.42 wt % (Table S6), which is similar to previous reports of apatite compositions in NWA 7034 [*Agee et al*., 2013; *Humayun et al*., 2013; *McCubbin et al*., 2016; *Muttik et al*., 2014; *Nyquist et al*., 2016; *Santos et al*., 2015; *Williams et al*., 2016]. In fact, many of the apatites measured for U-Pb in the present study were the same grains used by *Williams et al*. [2016] to determine the chlorine isotopic composition of apatites in NWA 7034. Trace element analyses, including U and Th, were determined by using the SHRIMP-RG. All of the apatites were light rare earth element-enriched with La/Yb values from 2.4 to 15.1 (Table S8). The U and Th abundances ranged from 0.6 to 23.7 ppm and 1.4 to 200.6 ppm, respectively (Table S7). The U-Pb data from all of the apatite were plotted on a Tera-Wasserburg concordia diagram, and the results indicate an age of 1.49 ± 0.09 Ga (Figure 11c).

## 5. Discussion

### 5.1. Evidence for Oxidized Alkalic Volcanism on Early Mars

Of the seven zircon grains that were dated by the U-Pb system, six of them were crystal clasts that were out of petrologic context. Only Zircon 6 was within an igneous textured clast, although Zircon 5 was also likely within the same clast. Zircon 6 yielded a weighted average $^{207}Pb/^{206}Pb$ date of 4.72 ± 0.23 Ga, a weighted average $^{207}Pb/^{235}U$ date of 4.39 ± 0.17 Ga, and a weighted average $^{206}Pb/^{238}U$ date of 3.70 ± 0.31 Ga (Table S3), which are fairly imprecise but consistently indicate an ancient crystallization age. The igneous clast that hosts Zircon 6 was petrologically characterized by *Santos et al*. [2015] as a basalt with 48.76 wt % $SiO_2$, and it is identified as Clast 78. Clast 78 has 3.06 wt % $Na_2O$ and 1.82 wt % $K_2O$, which distinguishes this clast as an alkali basalt. In fact, the age of the zircon in this clast indicates that Clast 78 is the oldest basalt from Mars that has been dated in situ.

Alkali basalts are typically olivine-normative and do not contain low-Ca pyroxene, but olivine is not present within Clast 78 and it has approximately 12% low-Ca pyroxene [*Santos et al*., 2015]. In fact, the paucity of olivine in NWA 7034 is one of its primary distinguishing features [*Agee et al*., 2013; *Humayun et al*., 2013; *Santos et al*., 2015]. There is some debate as to the cause of the missing olivine in NWA 7034, and it is typically either attributed to elevated oxygen fugacity in the parental magmas [*Santos et al*., 2015] or secondary aqueous alteration/oxidation of olivine followed by impact melting and crystallization [*Humayun et al*., 2014]. Clast 78 has an $Fe^{3+}/\sum Fe$ of 0.23 [*Santos et al*., 2015], which is attributed to the abundance of Fe-Ti oxides

(magnetite and ilmenite) in the clast (Figure 10). Using the program QUILF [*Andersen et al*., 1993] and the Fe-Ti oxide analyses of Clast 78 from *Santos et al*. [2015] that exhibit an equilibrium distribution of Mg and Mn between ilmenite and magnetite [*Bacon and Hirschmann*, 1988], we estimate an $fO_2$ that is ~2 log units above the fayalite-magnetite-quartz buffer and an equilibration temperature of ~745°C (Figure 10). Given the ancient crystallization age of Clast 78 as well as its elevated $fO_2$, we attribute the paucity of olivine in this alkali basalt as a direct consequence of the elevated oxygen fugacity of the parental magmas. In addition, early oxidizing magmatism on Mars is supported by the compositions of ancient surface rocks analyzed by the Mars Exploration Rovers [*Schmidt et al*., 2013; *Tuff et al*., 2013].

Alkali basalts are absent among the much younger shergottite Martian meteorites, but there have been a number of rocks analyzed by Martian rovers that indicate the presence of alkali basalts and more evolved alkalic volcanism on Mars [*McSween et al*., 2006a, 2006b; *Sautter et al*., 2015, 2016; *Schmidt et al*., 2014; *Stolper et al*., 2013], and some melt inclusion compositions in the chassignites have been used to suggest the occurrence of alkalic volcanism on Mars [*Nekvasil et al*., 2007, 2009]. The ages of the alkali-rich surface rocks have not been determined, but they are inferred to be fairly ancient, ~3.65 Ga for the basalts in Gusev Crater [*Greeley et al*., 2005] and <3.86 Ga for the evolved volcanic rocks in Gale Crater [*Farley et al*., 2014; *Sautter et al*., 2015]. The age of the chassignites is younger at 1.3 Ga [*Nyquist et al*., 2001]. Although it is difficult to speculate about the origin of the alkali basalt lithologies on Mars without additional data, the ancient date of Zircon 6 in alkali basalt Clast 78 is further evidence that alkalic volcanism on Mars is correlated with ancient ages. This correlation is unsurprising because alkalis are incompatible elements and would be among the first elements to be depleted during partial melting of the mantle in the case of a primary origin for these lithologies. Alternatively, these lithologies could have arisen by crustal contamination of primary magmas by the earliest Martian crust, which is a substantial reservoir for alkalis [*McLennan*, 2001; *Taylor*, 2013; *Taylor et al*., 2010] and is postulated to have been oxidized very early [i.e., *Sharp et al*., 2013].

### 5.2. Identification of Precursor Matrix Materials in NWA 7034

The identity of the precursor materials to the submicron groundmass is presently unknown and difficult to discern given the thermal overprinting, but we can begin to place constraints based on the textural and chemical properties of the groundmass combined with knowledge of known Martian surface reservoirs. The submicron nature of the groundmass indicates that the precursor materials had to be composed of amorphous materials or extremely fine submicron dust because thermal processing only increases grain size. The vitrophyric clasts were almost certainly an amorphous glass precursor material based on their macroscopic textures and Fe-rich compositions [*Santos et al*., 2015; *Udry et al*., 2014] linking them to either volcanic- or impact-derived melt spherules. However, the origin of the groundmass material in the bulk matrix domain and the protobreccia clasts has a lower abundance of Fe and do not exhibit macroscopic textures consistent with a quenched melt.

The matrix materials in the bulk matrix domain and the protobreccia clasts could be linked to a Martian global dust component that is ubiquitous on the Martian surface and has been found globally in Martian soils [*Bish et al*., 2013; *Blake et al*., 2013; *Vaniman et al*., 2014]. Orbital and in situ measurements of this material display a remarkably homogeneous chemical composition and suggest that it consists of at least three phases: nanophase iron oxides [*Morris et al*., 2008], an amorphous silicate, consistent with altered volcanic glass, and an amorphous sulfate phase [*Chipera and Vaniman*, 2007; *Vaniman et al*., 2004]. These amorphous/poorly crystalline materials likely occur both as primary phases, such as volcanic and impact glasses, and as secondary phases, through the alteration of primary minerals [*Downs and Team*, 2015]. However, the composition of the bulk matrix domain of NWA 7034 and the matrix domain of the protobreccia clasts are a poor match for the global dust component on Mars [*Blake et al*., 2013; *Santos et al*., 2015]; however, they are similar in composition to soils from Gusev Crater analyzed by the Mars Exploration Rover, Spirit [*Gellert et al*., 2004, 2006; *Haskin et al*., 2005; *Yen et al*., 2005].

Another possibility is that the precursor materials are composed of dehydrogenated Martian alteration minerals that have been identified previously on the Martian surface such as clays, oxides, and carbonates [*Bibring et al*., 2006; *Ehlmann et al*., 2008, 2009; *Klingelhofer et al*., 2004; *Morris et al*., 2010; *Poulet et al*., 2005]. In particular, phyllosilicate-rich materials liberate OH and structurally bound $H_2O$ upon heating and could crystallize a mineral assemblage similar to that observed in the NWA 7034 matrices, including

pyroxene-, plagioclase-, and oxide-bearing assemblages depending on the compositions of the clays. However, we note that there is no strong evidence to support this scenario given the absence of evidence of fluid alteration within many of the lithic clasts, which would have been hydrothermally altered by the liberated $H_2O$-rich fluid. Importantly, we do not consider the identification of minor saponitic clay as supporting evidence for this model because a terrestrial origin for the saponite cannot be excluded.

The final possibility we consider is that the precursor materials to the bulk matrix of NWA 7034 represent a pulverized mixture of crustal rocks ranging in grain size from approximately 1 μm up to several millimeters, and the fine-grained submicron matrix primarily represents reworked amorphous volcanic and impact glasses with lesser amounts of dehydrogenated alteration minerals. This scenario is somewhat intermediate between the first two scenarios, but there are a number of lines of evidence that support this scenario. First, there is a strong consistency between the major element composition of the bulk matrix domain and the average Martian crust, particularly in the southern highlands [*Agee et al*., 2013; *Humayun et al*., 2013; *McCubbin et al*., 2015; *Santos et al*., 2015]. Furthermore, NWA 7034 yields a better match than any other Martian meteorite to visible-infrared reflectance spectra of the Martian surface measured from orbit [*Beck et al*., 2015; *Cannon et al*., 2015]. Lastly, the mineral assemblages in the submicron groundmass are very similar, in both composition and mineralogy, to the larger crystal clasts within the bulk matrix domain of NWA 7034 [*Muttik et al*., 2014; *Nyquist et al*., 2016; *Santos et al*., 2015]. Consequently, we infer that the bulk matrix domain of NWA 7034 is composed of pulverized crustal material and devitrified amorphous materials that have been sufficiently mixed to the point that they represent a good match to the bulk composition of the Martian crust, similar to terrestrial loess on Earth; however, we note that this material is compositionally distinct from the global dust component analyzed in Gale Crater [*Blake et al*., 2013].

### 5.3. Lithification of NWA 7034: Textural Evidence of Thermal Processing

The textures exhibited by the bulk matrix domain at the submicrometer scale within NWA 7034 provide evidence of secondary thermal processing that resulted in partial equilibration of the groundmass materials. This equilibration is characterized by micron to submicron-sized equigranular crystals of plagioclase, pyroxene, magnetite, ilmenite, and Cl-rich apatite that commonly meet at 120° triple junctions (Figures 2 and 3). The submicrometer grain sizes of the bulk matrix domain suggest, qualitatively, that the heating event responsible for the partial equilibration was either at a high temperature (700–800°C) for a short duration or at mild-moderate temperature (500–700°C) for a long duration, otherwise substantial grain coarsening would have occurred in the bulk matrix domain. Evidence for this thermal event is present throughout the NWA 7034 breccia, based on textures exhibited by the submicron groundmass in a number of clasts hosted by the bulk matrix domain, including the vitrophyric clast as well as the matrix within the protobreccia clasts.

Given the fine-grained, possibly amorphous precursor starting materials of the NWA 7034 groundmass, temperature estimates for the thermal event are comparable to sintering/heating experiments on GEMS (glass with embedded metal and sulfides), which are the major primitive components of interplanetary dust particles. GEMS grains are $<0.5$ μm in diameter objects that consist of numerous 10 to 50 nm sized FeNi metal and Fe-Ni sulfide grains dispersed in a Mg-Si-Al-Fe amorphous silicate matrix [*Bradley*, 1994; *Keller and Messenger*, 2011]. TEM investigations of GEMs show heat-related changes at 700°C and severe transformation at temperatures between 800 and 850°C that leads to melting [*Brownlee et al*., 2005]. At just about 700°C the typical GEMS texture of silicate glass with fine embedded metal and sulfide transforms to an igneous-like texture of silica rich glass and prominent subhedral to euhedral grains of moderately iron-rich olivine and pyroxene. Based on the experimental results for thermally altered GEMS, the secondary thermal annealing/sintering in NWA 7034 is consistent with a maximum equilibration temperature of approximately 800°C because we do not observe evidence of partial melting in the submicron portions of NWA 7034. The textures exhibited by the submicron groundmass in NWA 7034 are most similar to the experimental results exhibited by thermal alteration of GEMS at 700°C; however, we cannot use this result to further constrain the temperature of the thermal event that annealed NWA 7034 because the duration of the heating event in NWA 7034 is unknown.

### 5.4. Hydrothermal Activity in the Protobreccia Clasts

As discussed previously, the protobreccia clasts represent a prior generation of Martian regolith that has been through the thermal cycling process of regolith formation prior to the formation of the NWA 7034

breccia. The additional thermal cycling is evident by the coarser grain sizes in the protobreccia matrix compared to the bulk matrix domain and the vitrophyric clast (Figure 5). However, the large medium-gravel protobreccia clast in NWA 7034 thin section 2,2 also exhibits strong evidence of having been hydrothermally altered prior to incorporation into the sediments that later lithified to become the bulk matrix domain of NWA 7034. This evidence is characterized by (1) veining of magnetite throughout the clast that crosscuts crystalline clasts and groundmass in the protobreccia, (2) pyrite-pyroxene intergrowths in some crystal clasts within the protobreccia clast, and (3) the presence of patchy secondary Fe-oxides in portions of the groundmass and within several crystal clasts. Of these three observations, the magnetite veins provide the strongest textural information with respect to the timing of hydrothermal activity. All of the magnetite veins either terminate at or before the edge of the protobreccia clast, and the veins crosscut existing clasts in the protobreccia (Figures 5 and 6). Both of these observations indicate that the hydrothermal alteration occurred prior to the incorporation of the protobreccia gravel into the sediments that would become the bulk matrix domain of NWA 7034. Furthermore, the hydrothermal activity must have occurred after the lithification of the protobreccia. Given the thermal overprinting that occurred during the lithification of NWA 7034, it is not possible to glean quantitative information on the properties of the hydrothermal fluid without a detailed textural, structural, mineralogical, and chemical study of the alteration domains in the protobreccia clast, which is considered to be beyond the scope of the present study. However, this would be a promising area of future work.

### 5.5. Thermochronology of NWA 7034

The single zircon crystal clast analyzed from the NWA 7034 groundmass (Zircon 4) yielded a concordant U-Pb date of 4.39 ± 0.04 Ga (weighted average $^{207}Pb/^{206}Pb$ date from 5 NanoSIMS analyses and 1 SHRIMP-RG analysis; Tables S2 and S3 and Figure 11a), consistent with previous ancient ages reported for the groundmass materials in NWA 7034 from Sm-Nd isotopic systematics [*Nyquist et al*., 2016] and previously analyzed zircons [*Humayun et al*., 2013; *Nemchin et al*., 2014]. Two baddeleyite crystal clasts hosted by the bulk matrix domain yielded $^{207}Pb/^{206}Pb$ dates of ~4.3–4.4 Ga (Table S5), which is consistent with the zircon results. These results indicate that the materials hosted by the bulk matrix domain are ancient and comprise the oldest known Martian crust. Given the overlap in ancient ages for the Sm-Nd and U-Pb systems for the bulk matrix domain, we conclude that the materials that make up the bulk matrix domain have not undergone sufficient thermal processing to reset the ancient ages, which implies that this material remained below approximately 900°C [i.e., *Lee et al*., 1997] since 4.3–4.4 Ga. However, the textures imprinted on the submicron groundmass of the bulk matrix domain of NWA 7034 are consistent with a maximum sustained temperature of approximately 800°C within the last 4.4 Ga.

The correlation between young or discordant zircon dates, elevated abundances of U (Figure S11), and apparent radiation damage suggests that the 1.5 Ga dates of the zircon resulted from a thermal resetting event subsequent to initial zircon crystallization. The process of metamictization causes the closure temperature of zircon in the U-Pb system to decrease substantially from the typical value of >900°C [*Lee et al*., 1997], with self-annealing temperatures as low as 150°C [*Meldrum et al*., 1998; *Mezger and Krogstad*, 1997], leaving the U-rich zircons more susceptible to resetting during a thermal pulse. Consequently, the young dates at 1.5 Ga of the U-rich zircons are likely dating a thermal event, in which Pb was lost from the metamict zircons but retained in the highly crystalline zircons in the groundmass. All of the young zircons were within a single medium-gravel-sized protobreccia clast, which exhibits evidence of hydrothermal alteration prior to its incorporation into NWA 7034, so we could not use our zircon U-Pb results to determine whether or not the Pb-loss event was a specific event experienced solely by the protobreccia clast prior to its incorporation into NWA 7034 or a thermal event that occurred after the deposition of NWA 7034. However, U-Pb dates of apatite were determined for several textural domains in the present study, and it has a fairly low closure temperature (i.e., ~500°C [*Dahl*, 1997]), below that of the maximum thermal annealing estimate of 800°C, so apatite can be used to constrain the temperature of annealing.

The U-Pb data for apatite grains across all parts of the NWA 7034 sample (Figures S12–S15) record an ~1.5 Ga date (Figure 11c and Table S7). We interpret the young date of the apatite across the entire NWA 7034 breccia as evidence that a breccia-wide thermal event occurred at 1.5 ± 0.1 Ga, likely coinciding with the heating event that lithified the breccia and caused the interlocking, thermally equilibrated texture exhibited by the submicron groundmass in the bulk matrix domain of NWA 7034 (Figures 1 and 3). Furthermore, the temperature of this breccia-wide heating event is constrained to the range of 500–800°C. Importantly, this interpretation is

supported by a bulk rock K-Ar study (closure temperature in K-feldspar ≤ 300°C [*Foland*, 1974]) of NWA 7034 that recorded a gas retention age of approximately 1.56 Ga [*Cartwright et al*., 2014], which is an upper limit based on the assumption that all $^{40}$Ar is radiogenic.

The heating event recorded throughout the NWA 7034 breccia at 1.5 Ga has overprinted any age information that may have been recorded for the hydrothermal activity in the medium-gravel-sized protobreccia clast. Consequently, the only age constraint we can place regarding the timing of that hydrothermal activity is that it occurred between 1.5 and 4.4 Ga.

### 5.6. Depositional Process Responsible for NWA 7034

Based on the size and shape analysis, we can determine the process responsible for the deposition of NWA 7034. The size and shape measures vary somewhat with the different particle classes; however, they are not statistically different; thus, we may infer that while these clasts may have been emplaced at different times and/or from different sources, they were likely emplaced by the same general process. There is one terrestrial sedimentary deposit type that matches all of the observed particle size and shape characteristics described here: pyroclastic falls. These deposits result from explosive volcanic eruptions that eject lithic fragments, which then settle out of the atmosphere [*Kaminski and Jaupart*, 1998; *Walker*, 1971]. Measured mean and standard deviation of particle size for the Martian lithic clasts fall within the range of observed terrestrial volcanic pyroclastic fall deposits (fine gravel and sand [*Walker*, 1971]). These deposits exhibit a power law tail with $\gamma = 4.0–4.9$, but often deviate from this trend for particles smaller than 0.5 mm due to atmospheric loss of ash and finer pumice [*Kaminski and Jaupart*, 1998]. In addition, pyroclasts exhibit sharp, angular, and widely varying shapes, characteristic of fragments [*Manga et al*., 2011]. Our size and shape data strongly suggest that the clasts in NWA 7034 resulted from atmospheric deposition of fragmented rock. Collisional abrasion must have been negligible due to observed nonroundness, which rules out gravity-driven pyroclastic flows [*Manga et al*., 2011], while the poor sorting goes against a base-surge interpretation [*Wittmann et al*., 2015]. Although NWA 7034 could have resulted from a volcanic pyroclastic fall, this scenario is likely excluded due to the ancient crystallization ages (~4.4 Ga) of many of the breccia components (*Humayun et al*. [2013], *Nyquist et al*. [2016], and the present study) and the comparitively young age of breccia lithification (~1.5 Ga). However, atmospheric rainout of fragments created by an asteroid or cometary impact would be similar to an explosive volcanic eruption, where the excavated material consists of a mixture of target rocks, so we infer that impact processes were likely responsible for the mobilization and heating of clastic materials that were deposited and subsequently lithified to form the NWA 7034 breccia.

## 6. Conclusions: Provenance of NWA 7034 and Implications for Mars

The nonmetamict zircon grains and baddeleyite yield U-Pb dates of approximately 4.3–4.4 Ga [*Humayun et al*., 2013] (Figure 11 and Table S5), and Sm-Nd data from igneous components in NWA 7034 indicate they are equally ancient [*Nyquist et al*., 2016]. Consequently, we conclude that the Martian meteorite NWA 7034 is primarily composed of ancient crustal materials from Mars that crystallized as early as 4.4 Ga. Despite the ancient age, K-Ar bulk rock data [*Cartwright et al*., 2014], U-Pb data in apatite (Figure 11c), U-Pb data in metamict zircon (Figures 11a and 11b), and the granoblastic texture exhibited by the submicron groundmass (Figures 1 and 3) all indicate that thermal processing has occurred since the crystallization of these phases. In fact, the concordance of dates at ~1.5 Ga from radiogenic systems with closure temperatures < 900°C argue strongly that the NWA 7034 breccia was lithified by thermal annealing at or before that time. The ~1.5 Ga mineral ages are interpreted to date the lithification of NWA 7034 because there is no evidence of earlier high-temperature recrystallization and/or Pb-loss for the 4.4 Ga populations of zircon and baddeleyite. Moreover, the high degree of preservation of primary igneous 4.4 Ga textures [*Santos et al*., 2015] precludes a pervasive high-temperature recrystallization history prior to 1.5 Ga. The submicron nature of the bulk matrix groundmass provides permissive evidence that the heating event at ~1.5 Ga was concomitant with lithification, otherwise grain sizes would have likely coarsened beyond submicron crystal sizes in the bulk matrix domain, and delicate vitrophyric clast textures would be altered. In fact, the coarser grain size of the groundmass in the protobreccia clasts attests to the additional thermal processing that occurred during its initial lithification. We are unable to definitively determine the source of heat for this event, but the grain shape and size distributions of the clasts indicate that they were deposited by atmospheric rainout of hot volcanic or impact-ejecta materials, as both impact and

volcanic processes operated on Mars at 1.5 Ga [*Nyquist et al*., 2001; *Schon and Head*, 2012]. However, given the ancient igneous crystallization ages for much of these materials (*Humayun et al*. [2013], *Nyquist et al*. [2016], and the present study), it would seem that impact processes were more likely the dominant mechanism for generating NWA 7034 and its pairings. Impact processes have also been implicated in the formation of NWA 7034 based on the highly siderophile element systematics in NWA 7034 and its pairings [i.e., *Goderis et al*., 2016].

The presence of protobreccia clasts within NWA 7034 indicates that the process of thermal annealing of Martian regolith materials by impact and/or volcanic processes is common on Mars and is likely to be an important mechanism for the formation of sedimentary rocks on the Martian surface, at least during the Amazonian Epoch. Our findings are consistent with Mars having a cold and dry climate during the Amazonian Epoch due to the prevalence of minerals that are susceptible to aqueous alteration in NWA 7034 (i.e., apatite and pyroxene), although some aqueous alteration, consistent with low water:rock ratios, is observed [*Muttik et al*., 2014; *Liu et al*., 2016]. It is difficult to assess Martian surface environments (e.g., climate and habitability) before 1.5 Ga from NWA 7034 due to its complex thermal history, although the bimodal population of U-Pb ages is remarkable given that crustal fragments date to the oldest known crust of Mars and yet only appear to have experienced high-temperature metamorphism once at 1.5 Ga. This points to southern highlands source terrains for NWA 7034 that were static for up to billions of years outside the two episodes of impact reworking; at 1.5 Ga and the 0.008 Ga meteorite launch event. In fact, NWA 7034 has provided important insights into the types of samples to be selected for future Mars sample return missions. In particular, we should avoid surface samples from Mars that have undergone extensive thermal processing because the earliest low-temperature geologic history of Mars is likely to be disturbed and/or erased. Nevertheless, NWA 7034 has provided valuable clues to the petrogenetic environments of its earliest crust, the formation processes of the Martian regolith, and the Martian sedimentary environments during the Amazonian Epoch.

**Acknowledgments**

All of the data used in this study can be found within the contents of this manuscript or within the supporting information, which contain Figures S1–S15 and Tables S1–S8. We acknowledge the curatorial staff at the Institute of Meteoritics for allowing the use of thin sections of NWA 7034 during this study. We would also like to thank Seth Burgess, Arya Udry, and Axel Wittman for their constructive reviews that helped to improve the quality and clarity of the manuscript. We also want to thank Justin Filiberto for the editorial handling of the manuscript. We also acknowledge the efforts of two anonymous reviewers that provided important feedback on a prior verssion of this manuscript. This work was supported by the NASA Mars Fundamental Research Program grant NNX13AK44G awarded to F.M.M. J.W.B. acknowledges support from a NASA Early Career Fellowship (NNX13AG40G). C.K.S., A.S., and C.B.A. acknowledge support from the NASA Cosmochemistry Program (NNX13AH85G to C.K.S. and NNX14AI23G to C.B.A.). G.D. and T.N.S. acknowledge Hungarian NKFIH grant 119245 and T.N.S. also acknowledges support by the Imre Korányi Fellowship. R.T. and M.A. acknowledge financial support from a UK Science and Technology Facilities Council research grant (#ST/I001298/1) to M.A.. NSERC Discovery Grant funding to D.E.M. is gratefully acknowledged. Any use of trade, firm, or product names is for descriptive purposes only and does not imply endorsement by the U.S. Government.

## References

Adcock, C. T., E. M. Hausrath, and P. M. Forster (2013), Readily available phosphate from minerals in early aqueous environments on Mars, *Nat. Geosci.*, *6*, 824–827.

Agee, C. B., et al. (2013), Unique meteorite from Early Amazonian Mars: Water-rich basaltic breccia Northwest Africa 7034, *Science*, *339*, 780–785.

Andersen, D. J., D. H. Lindsley, and P. M. Davidson (1993), QUILF—A Pascal program to assess equilibria among Fe-Mg-Mn-Ti oxides, pyroxenes, olivine, and quartz, *Comput. Geosci.*, *19*, 1333–1350.

Aström, J. A. (2006), Statistical models of brittle fragmentation, *Adv. Phys.*, *55*, 247–278.

Bacon, C. R., and M. M. Hirschmann (1988), Mg/Mn partitioning as a test for equilibrium between coexisting Fe-Ti oxides, *Am. Mineral.*, *73*, 57–61.

Bagnold, R. A. (1941), *The Physics of Blown Sand and Desert Dunes*, 265 pp., Methuen, London.

Beck, P., et al. (2015), A Noachian source region for the "Black Beauty" meteorite, and a source lithology for Mars surface hydrated dust?, *Earth Planet. Sci. Lett.*, *427*, 104–111.

Bellucci, J. J., A. A. Nemchin, M. J. Whitehouse, M. Humayun, R. Hewins, and B. Zanda (2015), Pb-isotopic evidence for an early, enriched crust on Mars, *Earth Planet. Sci. Lett.*, *410*, 34–41.

Bibring, J. P., et al. (2005), Mars surface diversity as revealed by the OMEGA/Mars Express observations, *Science*, *307*, 1576–1581.

Bibring, J. P., et al. (2006), Global mineralogical and aqueous mars history derived from OMEGA/Mars express data, *Science*, *312*, 400–404.

Bish, D. L., et al. (2013), X-ray diffraction results from Mars Science Laboratory: Mineralogy of Rocknest at Gale Crater, *Science*, *341*(6153), doi:10.1126/science.1238932.

Blake, D. F., et al. (2013), Curiosity at Gale Crater, Mars: Characterization and analysis of the Rocknest sand shadow, *Science*, *341*(6153), doi:10.1126/science.1239505.

Blott, S. J., and K. Pye (2008), Particle shape: A review and new methods of characterization and classification, *Sedimentology*, *55*, 31–63.

Borg, L. E., and D. S. Draper (2003), A petrogenetic model for the origin and compositional variation of the Martian basaltic meteorites, *Meteorit. Planet. Sci.*, *38*, 1713–1731.

Bradley, J. P. (1994), Chemically anomalous, preaccretionally irradiated grains in interplanetary dust from comets, *Science*, *265*, 925–929.

Brandon, A. D., I. S. Puchtel, R. J. Walker, J. M. D. Day, A. J. Irving, and L. A. Taylor (2012), Evolution of the Martian mantle inferred from the $^{187}$Re-$^{187}$Os isotope and highly siderophile element abundance systematics of shergottite meteorites, *Geochim. Cosmochim. Acta*, *76*, 206–235.

Brownlee, D. E., D. J. Joswiak, J. P. Bradley, G. Matrajt, and D. H. Wooden (2005), Cooked GEMS: Insights into the hot origin of crystalline silicates in circumstellar disks and the cold origin of GEMS paper presented at Proc. Lunar Planet. Sci. Conf. 36th, Lunar Planet. Inst., Houston, Tex.

Cannon, K. M., J. F. Mustard, and C. B. Agee (2015), Evidence for a widespread basaltic breccia component in the Martian low-albedo regions from the reflectance spectrum of Northwest Africa 7034, *Icarus*, *252*, 150–153.

Carr, M. H. (2007), *The Surface of Mars*, Cambridge Univ. Press, New York.

Cartwright, J. A., U. Ott, S. Herrmann, and C. B. Agee (2014), Modern atmospheric signatures in 4.4 Ga Martian meteorite NWA 7034, *Earth Planet. Sci. Lett.*, *400*, 77–87.

Chipera, S. J., and D. T. Vaniman (2007), Experimental stability of magnesium sulfate hydrates that may be present on Mars, *Geochim. Cosmochim. Acta*, *71*, 241–250.

Christensen, P. R., et al. (2005), Evidence for magmatic evolution and diversity on Mars from infrared observations, *Nature*, *436*, 504–509.

Claoué-Long, J. C., W. Compston, J. Roberts, and C. M. Fanning (1995), Two Carboniferous ages: A comparison of SHRIMP zircon dating with conventional zircon ages and $^{40}$Ar/$^{39}$Ar analysis. Geochronology, Time Scales and Global Stratigraphic Correlation, in *Society for Sedimentary Geology*, *Spec. Publ.*, vol. 4, pp. 3–21, SEPM (Society for Sedimentary Geology), Tulsa, Okla.

Collinet, M., E. Medard, B. Charlier, J. Vander Auwera, and T. L. Grove (2015), Melting of the primitive Martian mantle at 0.5–2.2 GPa and the origin of basalts and alkaline rocks on Mars, *Earth Planet. Sci. Lett.*, *427*, 83–94.
Cooney, T. F., E. R. D. Scott, A. N. Krot, S. K. Sharma, and A. Yamaguchi (1999), Vibrational spectroscopic study of minerals in the Martian meteorite ALH84001, *Am. Mineral.*, *84*, 1569–1576.
Dahl, P. S. (1997), A crystal-chemical basis for Pb retention and fission-track annealing systematics in U-bearing minerals, with implications for geochronology, *Earth Planet. Sci. Lett.*, *150*, 277–290.
Day, J. M. D., L. A. Taylor, C. Floss, and H. Y. McSween (2006), Petrology and chemistry of MIL 03346 and its significance in understanding the petrogenesis of nakhlites on Mars, *Meteorit. Planet. Sci.*, *41*, 581–606.
Domokos, G., D. J. Jerolmack, A. A. Sipos, and A. Török (2014), How river rocks round: Resolving the shape-size paradox, *Plos One*, *9*, e88657.
Domokos, G., F. Kun, A. A. Sipos, and T. Szabó (2015), Universality of fragment shapes, *Sci. Rep.*, *5*, 9147.
Downs, R. T., and M. S. L. S. Team (2015), Determining mineralogy on Mars with the CheMin X-ray diffractometer, *Elements*, *11*, 45–50.
Dreibus, G., R. Haubold, W. Huisl, and B. Spettel (2008), The loss of K, REE, Th, and U from a Martian and a terrestrial basalt by acidic leaching, *Meteorit. Planet. Sci.*, *43*, 1895–1908.
Dyar, M. D., A. H. Treiman, C. M. Pieters, T. Hiroi, M. D. Lane, and V. O'Connor (2005), MIL03346, the most oxidized Martian meteorite: A first look at spectroscopy, petrography, and mineral chemistry, *J. Geophys. Res.*, *110*, E09005, doi:10.1029/2005JE002426.
Ehlmann, B. L., et al. (2008), Orbital identification of carbonate-bearing rocks on Mars, *Science*, *322*, 1828–1832.
Ehlmann, B. L., et al. (2009), Identification of hydrated silicate minerals on Mars using MRO-CRISM: Geologic context near Nili Fossae and implications for aqueous alteration, *J. Geophys. Res.*, *114*, E00D08, doi:10.1029/2009JE003339.
Farley, K. A., et al. (2014), In situ radiometric and exposure age dating of the Martian surface, *Science*, *343*(6169), doi:10.1126/science.1247166.
Filiberto, J. (2008), Experimental constraints on the parental liquid of the Chassigny meteorite: A possible link between the Chassigny meteorite and a Martian Gusev basalt, *Geochim. Cosmochim. Acta*, *72*, 690–701.
Filiberto, J., and R. Dasgupta (2011), $Fe^{2+}$-Mg partitioning between olivine and basaltic melts: Applications to genesis of olivine-phyric shergottites and conditions of melting in the Martian interior, *Earth Planet. Sci. Lett.*, *304*, 527–537.
Filiberto, J., R. Dasgupta, W. S. Kiefer, and A. H. Treiman (2010a), High pressure, near-liquidus phase equilibria of the Home Plate basalt Fastball and melting in the Martian mantle, *Geophys. Res. Lett.*, *37*, L13201, doi:10.1029/2010GL043999.
Filiberto, J., D. S. Musselwhite, J. Gross, K. Burgess, L. Le, and A. H. Treiman (2010b), Experimental petrology, crystallization history, and parental magma characteristics of olivine-phyric shergottite NWA 1068: Implications for the petrogenesis of "enriched" olivine-phyric shergottites, *Meteorit. Planet. Sci.*, *45*, 1258–1270.
Foland, K. A. (1974), $^{40}$Ar diffusion in homogenous orthoclase and an interpretation of ar diffusion in K-feldspars, *Geochim. Cosmochim. Acta*, *38*, 151–166.
Friedman, G. M. (1962), On sorting, sorting coefficients, and the lognormality of the grain-size distribution of sandstones, *J. Geol.*, *70*, 737–753.
Gattacceca, J., P. Rochette, R. B. Scorzelli, P. Munayco, C. Agee, Y. Quesnel, C. Cournede, and J. Geissman (2014), Martian meteorites and Martian magnetic anomalies: A new perspective from NWA 7034, *Geophys. Res. Lett.*, *41*, 4859–4864, doi:10.1002/2014GL060464.
Gellert, R., et al. (2004), Chemistry of rocks and soils in Gusev crater from the alpha particle x-ray spectrometer, *Science*, *305*, 829–832.
Gellert, R., et al. (2006), Alpha particle X-ray spectrometer (APXS): Results from Gusev crater and calibration report, *J. Geophys. Res.*, *111*, E02S05, doi:10.1029/2005JE002555.
Goderis, S., A. D. Brandon, B. Mayer, and M. Humayun (2016), Ancient impactor components preserved and reworked in Martian regolith breccia Northwest Africa 7034, *Geochim. Cosmochim. Acta*, *191*, 203–215.
Golden, D. C., D. W. Ming, R. V. Morris, and S. A. Mertzman (2005), Laboratory-simulated acid-sulfate weathering of basaltic materials: Implications for formation of sulfates at Meridiani Planum and Gusev crater, Mars, *J. Geophys. Res.*, *110*, E12S07, doi:10.1029/2005JE002451.
Greeley, R., B. H. Foing, H. Y. McSween, G. Neukum, P. Pinet, M. van Kan, S. C. Werner, D. A. Williams, and T. E. Zegers (2005), Fluid lava flows in Gusev crater, Mars, *J. Geophys. Res.*, *110*, E05008, doi:10.1029/2005JE002401.
Greenwood, J. P., S. Itoh, N. Sakamoto, E. P. Vicenzi, and H. Yurimoto (2008), Hydrogen isotope evidence for loss of water from Mars through time, *Geophys. Res. Lett.*, *35*, L05203, doi:10.1029/2007GL032721.
Grimes, C. B., B. E. John, P. B. Kelemen, F. K. Mazdab, J. L. Wooden, M. J. Cheadle, K. Hanghoj, and J. J. Schwartz (2007), Trace element chemistry of zircons from oceanic crust: A method for distinguishing detrital zircon provenance, *Geology*, *35*, 643–646.
Grotzinger, J. P., and R. E. Milliken (2012), The sedimentary rock record of Mars: Distribution, origins, and global stratigraphy, in *Sedimentary Geology of Mars*, edited by J. P. Grotzinger and R. E. Milliken, pp. 1–48, SEPM (Society for Sedimentary Geology), Tulsa, Okla.
Hartmann, W. K. (1969), Terrestrial, Lunar, and interplanetary rock fragmentation, *Icarus*, *10*, 201–203.
Haskin, L. A., et al. (2005), Water alteration of rocks and soils on Mars at the Spirit rover site in Gusev crater, *Nature*, *436*, 66–69.
Heaman, L. M. (2009), The application of U-Pb geochronology to mafic, ultramafic and alkaline rocks: An evaluation of three mineral standards, *Chem. Geol.*, *261*, 42–51.
Herd, C. D. K., L. E. Borg, J. H. Jones, and J. J. Papike (2002), Oxygen fugacity and geochemical variations in the Martian basalts: Implications for Martian basalt petrogenesis and the oxidation state of the upper mantle of Mars, *Geochim. Cosmochim. Acta*, *66*, 2025–2036.
Hiess, J., A. P. Nutman, V. C. Bennett, and P. Holden (2008), Ti-in-zircon thermometry applied to contrasting Archean metamorphic and igneous systems, *Chem. Geol.*, *247*, 323–338.
Hiess, J., D. J. Condon, N. McLean, and S. R. Noble (2012), $^{238}$U/$^{235}$U systematics in terrestrial uranium-bearing minerals, *Science*, *335*, 1610–1614.
Humayun, M., et al. (2013), Origin and age of the earliest Martian crust from meteorite NWA 7533, *Nature*, *503*, 513–516.
Humayun, M., A. Nemchin, B. Zanda, and R. H. Hewins (2014), The differentiation of the Martian highlands from NWA 7533 paper presented at Proceedings of the 2014 Goldschmidt Conference, Sacramento, Calif.
Hurowitz, J. A., S. M. McLennan, D. H. Lindsley, and M. A. A. Schoonen (2005), Experimental epithermal alteration of synthetic Los Angeles meteorite: Implications for the origin of Martian soils and identification of hydrothermal sites on Mars, *J. Geophys. Res.*, *110*, E07002, doi:10.1029/2004JE002391.
Jerolmack, D. J., M. D. Reitz, and R. L. Martin (2011), Sorting out abrasion in a gypsum dune field, *J. Geophys. Res.*, *116*, F02003, doi:10.1029/2010JF001821.
Jutzeler, M., A. A. Proussevitch, and S. R. Allen (2012), Grain-size distribution of volcaniclastic rocks 1: A new technique based on functional stereology, *J. Volcanol. Geotherm. Res.*, *239*, 1–11.
Kaminski, E., and C. Jaupart (1998), The size distribution of pyroclasts and the fragmentation sequence in explosive volcanic eruptions, *J. Geophys. Res.*, *103*, 29,759–29,779, doi:10.1029/98JB02795.
Kekäläinen, P., J. A. Aström, and J. Timonen (2007), Solution for the fragment-size distribution in a crack-branching model of fragmentation, *Phys. Rev. E*, *76*, 026112.

Keller, L. P., and S. Messenger (2011), On the origins of GEMS grains, *Geochim. Cosmochim. Acta*, *75*, 5336–5365.
Klingelhofer, G., et al. (2004), Jarosite and hematite at Meridiani Planum from Opportunity's Mossbauer spectrometer, *Science*, *306*, 1740–1745.
Lee, J. K. W., I. S. Williams, and D. J. Ellis (1997), Pb, U and Th diffusion in natural zircon, *Nature*, *390*, 159–162.
Leroux, H., D. Jacob, M. Marinova, R. H. Hewins, B. Zanda, S. Pont, J.-P. Lorand, and M. Humayun (2016), Exsolution and shock microstructures of igneous pyroxene clasts in the Northwest Africa 7533 Martian meteorite, *Meteorit. Planet. Sci.*, *51*, 932–945.
Liu, Y., C. Ma, J. R. Beckett, Y. Chen, and Y. B. Guan (2016), Rare-earth-element minerals in martian breccia meteorites NWA 7034 and 7533: Implications for fluid-rock interaction in the martian crust, *Earth Planet. Sci. Lett.*, *451*, 251–262.
Lorand, J. P., et al. (2015), Nickeliferous pyrite tracks pervasive hydrothermal alteration in Martian regolith breccia: A study in NWA 7533, *Meteorit. Planet. Sci.*, *50*, 2099–2120.
Ludwig, K. R. (2008), *Isoplot/Ex Version 3.70: A Geochronological Toolkit for Microsoft Excel*, *Spec. Publ.*, vol. 4, 73 pp., Berkeley Geochronology Center, Berkeley Calif. [Available at http://www.bgc.org/isoplot_etc/isoplot.html.]
Ludwig, K. R. (2009), *Squid 2: A User's Manual*, 95 pp., Berkeley Geochronology Center, Berkeley Calif. [Available at http://www.bgc.org/isoplot_etc/squid.html.]
Malin, M. C., and K. S. Edgett (2000), Sedimentary rocks of early Mars, *Science*, *290*, 1927–1937.
Manga, M., A. Patel, and J. Dufek (2011), Rounding of pumice clasts during transport: Field measurements and laboratory studies, *Bull. Volcanol.*, *73*, 321–333.
Mattinson, J. M. (2010), Analysis of the relative decay constants of $^{235}$U and $^{238}$U by multi-step CA-TIMS measurements of closed-system natural zircon samples, *Chem. Geol.*, *275*, 186–198.
McCanta, M. C., M. J. Rutherford, and J. H. Jones (2004), An experimental study of rare earth element partitioning between a shergottite melt and pigeonite: Implications for the oxygen fugacity of the Martian interior, *Geochim. Cosmochim. Acta*, *68*, 1943–1952.
McCubbin, F. M., H. Nekvasil, A. D. Harrington, S. M. Elardo, and D. H. Lindsley (2008), Compositional diversity and stratification of the Martian crust: Inferences from crystallization experiments on the picrobasalt Humphrey from Gusev Crater, Mars, *J. Geophys. Res.*, *113*, E11013, doi:10.1029/2008JE003165.
McCubbin, F. M., A. Steele, H. Nekvasil, A. Schnieders, T. Rose, M. Fries, P. K. Carpenter, and B. L. Jolliff (2010), Detection of structurally bound hydroxyl in fluorapatite from Apollo mare basalt 15058,128 using TOF-SIMS, *Am. Mineral.*, *95*, 1141–1150.
McCubbin, F. M., B. L. Jolliff, H. Nekvasil, P. K. Carpenter, R. A. Zeigler, A. Steele, S. M. Elardo, and D. H. Lindsley (2011), Fluorine and chlorine abundances in lunar apatite: Implications for heterogeneous distributions of magmatic volatiles in the lunar interior, *Geochim. Cosmochim. Acta*, *75*, 5073–5093.
McCubbin, F. M., S. M. Elardo, C. K. Shearer Jr., A. Smirnov, E. H. Hauri, and D. S. Draper (2013), A petrogenetic model for the co-magmatic origin of chassignites and nakhlites: Inferences from chlorine-rich minerals, petrology, and geochemistry, *Meteorit. Planet. Sci.*, *48*, 819–853.
McCubbin, F. M., A. Simonetti, C. K. Shearer Jr., A. R. Santos, J. M. D. Day, J. W. Boyce, N. Muttik, and C. B. Agee (2015), Composition of fine-grained bulk matrix and protobreccia clast matrix in Northwest Africa 7034: Implications for the composition of the Martian crust paper presented at Proc. Lunar Planet. Sci. Conf. 46th, Lunar Planet. Inst., Woodlands, Tex.
McCubbin, F. M., J. W. Boyce, P. Srinivasan, A. R. Santos, S. M. Elardo, J. Filiberto, A. Steele, and C. K. Shearer (2016), Heterogeneous distribution of $H_2O$ in the Martian interior: Implications for the abundance of $H_2O$ in depleted and enriched mantle sources, *Meteorit. Planet. Sci.*, doi:10.1111/maps.12639 in press.
McEwen, A. S., L. Ojha, C. M. Dundas, S. S. Mattson, S. Byrne, J. J. Wray, S. C. Cull, S. L. Murchie, N. Thomas, and V. C. Gulick (2011), Seasonal flows on warm Martian slopes, *Science*, *333*, 740–743.
McKay, D. S., E. K. Gibson, K. L. ThomasKeprta, H. Vali, C. S. Romanek, S. J. Clemett, X. D. F. Chillier, C. R. Maechling, and R. N. Zare (1996), Search for past life on Mars: Possible relic biogenic activity in Martian meteorite ALH84001, *Science*, *273*, 924–930.
McLennan, S. M. (2001), Crustal heat production and the thermal evolution of Mars, *Geophys. Res. Lett.*, *28*, 4019–4022, doi:10.1029/2001GL013743.
McLennan, S. M. (2012), Geochemistry of sedimentary processes on Mars, in *Sedimentary Geology of Mars*, edited by J. P. Grotzinger and R. E. Milliken, pp. 119–138, SEPM (Society for Sedimentary Geology), Tulsa, Okla.
McLennan, S. M., et al. (2005), Provenance and diagenesis of the evaporite-bearing Burns formation, Meridiani Planum, Mars, *Earth Planet. Sci. Lett.*, *240*, 95–121.
McLennan, S. M., et al. (2014), Elemental geochemistry of sedimentary rocks at Yellowknife Bay, Gale Crater, Mars, *Science*, *343*(6169), doi:10.1126/science.1244734.
McSween, H. Y., and A. H. Treiman (1998), Martian meteorites, in *Planetary Materials*, edited by J. J. Papike, pp. F1–F53, Mineral. Soc. Am., Washington, D. C.
McSween, H. Y., et al. (1999), Chemical, multispectral, and textural constraints on the composition and origin of rocks at the Mars Pathfinder landing site, *J. Geophys. Res.*, *104*(E4), 8679–8715, doi:10.1029/98JE02551.
McSween, H. Y., T. L. Grove, R. C. F. Lentz, J. C. Dann, A. H. Holzheid, L. R. Riciputi, and J. G. Ryan (2001), Geochemical evidence for magmatic water within Mars from pyroxenes in the Shergotty meteorite, *Nature*, *409*, 487–490.
McSween, H. Y., et al. (2004), Basaltic rocks analyzed by the Spirit rover in Gusev Crater, *Science*, *305*, 842–845.
McSween, H. Y., S. W. Ruff, R. V. Morris, J. F. Bell, K. E. Herkenhoff, R. Gellert, and A. S. Team (2006a), Backstay and Irvine: Alkaline volcanic rocks from Gusev Crater, Mars, paper presented at Proc. Lunar Planet. Sci. Conf. 37th, Houston, Tex.
McSween, H. Y., et al. (2006b), Alkaline volcanic rocks from the Columbia Hills, Gusev crater, Mars, *J. Geophys. Res.*, *111*, E09S91, doi:10.1029/2006JE002698.
McSween, H. Y., G. J. Taylor, and M. B. Wyatt (2009), Elemental composition of the Martian crust, *Science*, *324*, 736–739.
Medard, E., and T. L. Grove (2006), Early hydrous melting and degassing of the Martian interior, *J. Geophys. Res.*, *111*, E11003, doi:10.1029/2006JE002742.
Meldrum, A., L. A. Boatner, W. J. Weber, and R. C. Ewing (1998), Radiation damage in zircon and monazite, *Geochim. Cosmochim. Acta*, *62*, 2509–2520.
Mezger, K., and E. J. Krogstad (1997), Interpretation of discordant U-Pb zircon ages: An evaluation, *J. Metamorph. Geol.*, *15*, 127–140.
Monders, A. G., E. Medard, and T. L. Grove (2007), Phase equilibrium investigations of the Adirondack class basalts from the Gusev plains, Gusev crater, Mars, *Meteorit. Planet. Sci.*, *42*, 131–148.
Monkawa, A., T. Mikouchi, E. Koizumi, K. Sugiyama, and M. Miyamoto (2006), Determination of the Fe oxidation state of the Chassigny kaersutite: A microXANES spectroscopic study, *Meteorit. Planet. Sci.*, *41*, 1321–1329.
Morris, R. V., et al. (2008), Iron mineralogy and aqueous alteration from Husband Hill through Home Plate at Gusev Crater, Mars: Results from the Mossbauer instrument on the Spirit Mars Exploration Rover, *J. Geophys. Res.*, *113*, E12S42, doi:10.1029/2008JE003201.
Morris, R. V., et al. (2010), Identification of carbonate-rich outcrops on Mars by the Spirit Rover, *Science*, *329*, 421–424.

Moser, D. E., K. R. Chamberlain, K. T. Tait, A. K. Schmitt, J. R. Darling, I. R. Barker, and B. C. Hyde (2013), Solving the Martian meteorite age conundrum using micro-baddeleyite and launch-generated zircon, *Nature*, *499*, 454–457.

Murchie, S., et al. (2007), Compact Reconnaissance Imaging Spectrometer for Mars (CRISM) on Mars Reconnaissance Orbiter (MRO), *J. Geophys. Res.*, *112*, E05S03, doi:10.1029/2006JE002682.

Musselwhite, D. S., H. A. Dalton, W. S. Kiefer, and A. H. Treiman (2006), Experimental petrology of the basaltic shergottite Yamato-980459: Implications for the thermal structure of the Martian mantle, *Meteorit. Planet. Sci.*, *41*, 1271–1290.

Muttik, N., F. M. McCubbin, L. P. Keller, A. R. Santos, W. A. McCutcheon, P. P. Provencio, Z. Rahman, C. K. Shearer, J. W. Boyce, and C. B. Agee (2014), Inventory of $H_2O$ in the ancient Martian regolith from Northwest Africa 7034: The important role of Fe oxides, *Geophys. Res. Lett.*, *41*, 8235–8244, doi:10.1002/2014GL062533.

Nekvasil, H., J. Filiberto, F. M. McCubbin, and D. H. Lindsley (2007), Alkalic parental magmas for the chassignites? *Meteorit. Planet. Sci.*, *42*, 979–992.

Nekvasil, H., F. M. McCubbin, A. Harrington, S. Elardo, and D. H. Lindsley (2009), Linking the Chassigny meteorite and the Martian surface rock Backstay: Insights into igneous crustal differentiation processes on Mars, *Meteorit. Planet. Sci.*, *44*, 853–869.

Nemchin, A. A., M. Humayun, M. J. Whitehouse, R. H. Hewins, J. P. Lorand, A. Kennedy, M. Grange, B. Zanda, C. Fieni, and D. Deldicque (2014), Record of the ancient Martian hydrosphere and atmosphere preserved in zircon from a Martian meteorite, *Nat. Geosci.*, *7*, 638–642.

Nyquist, L. E., D. D. Bogard, C. Y. Shih, A. Greshake, D. Stoffler, and O. Eugster (2001), Ages and geologic histories of Martian meteorites, *Space Sci. Rev.*, *96*, 105–164.

Nyquist, L. E., C. Shih, F. M. McCubbin, A. R. Santos, C. K. Shearer Jr., Z. Peng, P. V. Burger, and C. B. Agee (2016), Rb-Sr and Sm-Nd isotopic and REE studies of igneous components in the bulk matrix domain of Martian breccia Northwest Africa 7034, *Meteorit. Planet. Sci.*, *51*, 483–498.

Papike, J. J., J. M. Karner, C. K. Shearer, and P. V. Burger (2009), Silicate mineralogy of Martian meteorites, *Geochim. Cosmochim. Acta*, *73*, 7443–7485.

Papike, J. J., P. V. Burger, C. K. Shearer, and F. M. McCubbin (2013), Experimental and crystal chemical study of the basalt–eclogite transition in Mars and implications for Martian magmatism, *Geochim. Cosmochim. Acta*, *104*, 358–376.

Poulet, F., J. P. Bibring, J. F. Mustard, A. Gendrin, N. Mangold, Y. Langevin, R. E. Arvidson, B. Gondet, C. Gomez, and T. Omega (2005), Phyllosilicates on Mars and implications for early Martian Martian Martian climate, *Nature*, *438*, 623–627.

Santos, A. R., C. B. Agee, F. M. McCubbin, C. K. Shearer, P. V. Burger, R. Tartese, and M. Anand (2015), Petrology of igneous clasts in Northwest Africa 7034: Implications for the petrologic diversity of the Martian crust, *Geochim. Cosmochim. Acta*, *157*, 56–85.

Sarbadhikari, A. B., J. M. D. Day, Y. Liu, D. Rumble, and L. A. Taylor (2009), Petrogenesis of olivine-phyric shergottite Larkman Nunatak 06319: Implications for enriched components in Martian basalts, *Geochim. Cosmochim. Acta*, *73*, 2190–2214.

Sautter, V., et al. (2015), In situ evidence for continental crust on early Mars, *Nat. Geosci.*, *8*, 605–609.

Sautter, V., et al. (2016), Magmatic complexity on early Mars as seen through a combination of orbital, in-situ and meteorite data, *Lithos*, *254–255*, 36–52.

Schmidt, M. E., C. M. Schrader, and T. J. McCoy (2013), The primary $fO_2$ of basalts examined by the Spirit rover in Gusev Crater, Mars: Evidence for multiple redox states in the Martian interior, *Earth MartianPlanet. Sci. Lett.*, *384*, 198–208.

Schmidt, M. E., et al. (2014), Geochemical diversity in first rocks examined by the Curiosity Rover in Gale Crater: Evidence for and significance of an alkali and volatile-rich igneous source, *J. Geophys. Res. Planets*, *119*, 64–81, doi:10.1002/2013JE004481.

Schoene, B., J. L. Crowley, D. J. Condon, M. D. Schmitz, and S. A. Bowring (2006), Reassessing the uranium decay constants for geochronology using ID-TIMS U-Pb data, *Geochim. Cosmochim. Acta*, *70*, 426–445.

Schon, S. C., and J. W. Head (2012), Gasa impact crater, Mars: Very young gullies formed from impact into latitude-dependent mantle and debris-covered glacier deposits? *Icarus*, *218*, 459–477.

Sha, L. K., and B. W. Chappell (1999), Apatite chemical composition, determined by electron microprobe and laser-ablation inductively coupled plasma mass spectrometry, as a probe into granite petrogenesis, *Geochim. Cosmochim. Acta*, *63*, 3861–3881.

Sharp, Z. D., F. M. McCubbin, and C. K. Shearer (2013), A hydrogen-based oxidation mechanism relevant to planetary formation, *Earth Planet. Sci. Lett.*, *380*, 88–97.

Shearer, C. K., P. M. Aaron, P. V. Burger, Y. Guan, A. S. Bell, and J. J. Papike (2013), Petrogenetic linkages among fO(2), isotopic enrichments-depletions and crystallization history in Martian basalts. Evidence from the distribution of phosphorus in olivine megacrysts, *Geochim. Cosmochim. Acta*, *120*, 17–38.

Shearer, C. K., P. V. Burger, J. J. Papike, F. M. McCubbin, and A. S. Bell (2015), Crystal chemistry of merrillite from Martian meteorites: Mineralogical recorders of magmatic processes and planetary differentiation, *Meteorit. Planet. Sci.*, *50*, 649–673.

Squyres, S. W., and A. H. Knoll (2005), Sedimentary rocks at Meridiani Planum: Origin, diagetiesis, and implications for life on Mars, *Earth Planet. Sci. Lett.*, *240*, 1–10.

Squyres, S. W., et al. (2004), In situ evidence for an ancient aqueous environment at Meridiani Planum, Mars, *Science*, *306*, 1709–1714.

Squyres, S. W., et al. (2006), Overview of the Opportunity Mars Exploration Rover mission to Meridiani Planum: Eagle crater to Purgatory ripple, *J. Geophys. Res.*, *111*, E12S12, doi:10.1029/2006JE002771.

Stacey, J. S., and J. D. Kramers (1975), Approximation of terrestrial lead isotope evolution by a 2-stage model, *Earth Planet. Sci. Lett.*, *26*, 207–221.

Steele, A., et al. (2012), A reduced organic carbon component in Martian basalts, *Science*, *337*, 212–215.

Stolper, E. M., et al. (2013), The petrochemistry of Jake_M: A Martian mugearite, *Science*, *341*(6153), doi:10.1126/science.1239463 .

Szabó, T., G. Domokos, J. P. Grotzinger, and D. J. Jerolmack (2015), Reconstructing the transport history of pebbles on Mars, *Nat. Commun.*, *6*, 8366–8366.

Tartèse, R., M. Anand, and T. Delhaye (2013), NanoSIMS Pb/Pb dating of tranquillityite in high-Ti lunar basalts: Implications for the chronology of high-Ti volcanism on the Moon, *Am. Mineral.*, *98*, 1477–1486.

Taylor, G. J. (2013), The bulk composition of Mars, *Chem. Erde-Geochem.*, *73*, 401–420.

Taylor, G. J., W. V. Boynton, S. M. McLennan, and L. M. V. Martel (2010), K and Cl concentrations on the Martian surface determined by the Mars Odyssey Gamma Ray Spectrometer: Implications for bulk halogen abundances in Mars, *Geophys. Res. Lett.*, *37*, L12204, doi:10.1029/2010GL043528.

Taylor, S. R., and S. M. McLennan (2008), *Planetary Crusts: Their Composition, Oigin and Evolution*, Cambridge Univ. Press, New York.

Terada, K., and Y. Sano (2003), In situ U-Pb dating and REE analyses of phosphates in extraterrestrial materials, *Appl. Surf. Sci.*, *203*, 810–813.

Terada, K., and Y. Sano (2012), *In-Situ* U–Pb dating of apatite by Hiroshima-SHRIMP: Contributions to Earth and planetary science, *Mass Spectrom.*, *1*, A0011, doi:10.5702/massspectrometry.A0011.

Thomson, S. N., G. E. Gehrels, J. Ruiz, and R. Buchwaldt (2012), Routine low-damage apatite U-Pb dating using laser ablation-multicollector-ICPMS, *Geochem. Geophys. Geosyst.*, *13*, Q0AA21, doi:10.1029/2011GC003928.

Tosca, N. J., and S. M. McLennan (2006), Chemical divides and evaporite assemblages on Mars, *Earth Planet. Sci. Lett.*, *241*, 21–31.
Treiman, A. H. (2005), The nakhlite meteorites: Augite-rich igneous rocks from Mars, *Chem. Erde-Geochem.*, *65*, 203–270.
Tuff, J., J. Wade, and B. J. Wood (2013), Volcanism on Mars controlled by early oxidation of the upper mantle, *Nature*, *498*, 342–345.
Udry, A., N. G. Lunning, H. Y. McSween Jr., and R. J. Bodnar (2014), Petrogenesis of a vitrophyre in the Martian meteorite breccia NWA 7034, *Geochim. Cosmochim. Acta*, *141*, 281–293.
Usui, T., H. Y. McSween, and C. Floss (2008), Petrogenesis of olivine-phyric shergottite Yamato 980459, revisited, *Geochim. Cosmochim. Acta*, *72*, 1711–1730.
Vaniman, D. T., D. L. Bish, S. J. Chipera, C. I. Fialips, J. W. Carey, and W. C. Feldman (2004), Magnesium sulphate salts and the history of water on Mars, *Nature*, *431*, 663–665.
Vaniman, D. T., et al. (2014), Mineralogy of a mudstone at Yellowknife Bay, Gale Crater, Mars, *Science*, *343*(6169), doi:10.1126/science.1243480 .
Wadhwa, M. (2001), Redox state of Mars' upper mantle and crust from Eu anomalies in shergottite pyroxenes, *Science*, *291*, 1527–1530.
Walker, G. P. L. (1971), Grain-size characteristics of pyroclastic deposits, *J. Geol.*, *79*, 696–714.
Wang, A., K. Kuebler, B. Jolliff, and L. A. Haskin (2004a), Mineralogy of a Martian meteorite as determined by Raman spectroscopy, *J. Raman Spectrosc.*, *35*, 504–514.
Wang, A., K. E. Kuebler, B. L. Jolliff, and L. A. Haskin (2004b), Raman spectroscopy of Fe-Ti-Cr-oxides, case study: Martian meteorite EETA79001, *Am. Mineral.*, *89*, 665–680.
Wiedenbeck, M., P. Alle, F. Corfu, W. L. Griffin, M. Meier, F. Oberli, A. Vonquadt, J. C. Roddick, and W. Speigel (1995), 3 natural zircon standards for U-Th-Pb, Lu-Hf, trace element, and REE analyses, *Geostand. Newsl.*, *19*, 1–23.
Wiedenbeck, M., et al. (2004), Further characterisation of the 91500 zircon crystal, *Geostand. Geoanal. Res.*, *28*, 9–39.
Williams, J. T., C. K. Shearer, Z. D. Sharp, P. V. Burger, F. M. McCubbin, A. R. Santos, C. B. Agee, and K. D. McKeegan (2016), The chlorine isotopic composition of Martian meteorites Part 1: Chlorine isotope composition of Martian mantle and crustal reservoirs and their interactions, *Meteorit. Planet. Sci.*, *51*, doi:10.1111/maps.12647 in press.
Wingate, M. T. D., and W. Compston (2000), Crystal orientation effects during ion microprobe U-Pb analysis of baddeleyite, *Chem. Geol.*, *168*, 75–97.
Wittmann, A., R. L. Korotev, B. L. Jolliff, A. J. Irving, D. E. Moser, I. Barker, and D. Rumble III (2015), Petrography and composition of Martian regolith breccia meteorite Northwest Africa 7475, *Meteorit. Planet. Sci.*, *50*, 326–352.
Yen, A. S., et al. (2005), An integrated view of the chemistry and mineralogy of Martian soils, *Nature*, *436*, 49–54.